Sonar Gas Flux Estimation by Bubble Insonification: Application to Methane Bubble Flux from the East Siberian Arctic Shelf

Ira Leifer[1,], Denis Chernykh[2,3], Natalia Shakhova[3,4], and Igor Semiletov[2,3,4]

[1] Bubbleology Research International, Solvang, CA 93463

[2] Russian Academy of Science, Pacific Oceanological Institute, Vladivostok, Russia

[3] National Tomsk Research Polytechnic University, Tomsk, Russia

[4] University Alaska Fairbanks, International Arctic Research Center, Fairbanks, USA

Abstract

Sonar surveys provide an effective mechanism for mapping seabed methane flux emissions, with Arctic submerged permafrost seepage having great potential to significantly affect climate. We created *in situ* engineered bubble plumes from 40-m depth with fluxes spanning 0.019 to 1.1 L/s to derive the *in situ* calibration curve, $Q(\sigma)$. Non-linear curves relating flux, Q, to sonar return, s, for a multibeam echosounder (MBES) and a single beam echosounder (SBES) for a range of depths demonstrated significant bubble-bubble acoustic interactions – precluding the use of a theoretical calibration function, $Q(\sigma)$, wherein bubble $\sigma(r)$ scales with the radius, r, size distribution. Bubble plume sonar occurrence probability distribution function, $\Psi(\sigma)$, with respect to Q found $\Psi(\sigma)$ for weak σ well described by a power law that likely correlated with small bubble dispersion and strongly depth dependent. $\Psi(\sigma)$ for strong s largely was depth-independent, consistent with bubble plume behavior where large bubbles in a plume remain in a focused core. As a result, $\Psi(\sigma)$ was bimodal for all but the weakest plumes.

$\Psi(\sigma)$ was applied to sonar observations of natural arctic Laptev Sea, seepage including accounting for volumetric change with a numerical bubble plume. Based on MBES data, values of total Q_m, the mass flux, were 5.56, 42.73, and 4.88 mmol/s with good to reasonable agreement between the SBES and MBES data (4-37%) for total Q. The seepage occurrence probability distribution function ($\Psi(Q)$) was bimodal, with weak $\Psi(Q)$ in each seep area well described by a power law, suggesting primarily minor bubble plumes. Seepage mapped spatial patterns suggested subsurface geologic control attributing methane fluxes to the current state of subsea permafrost.

Keywords: Bubble, multibeam sonar, single beam, quantification, Arctic, methane, submerged permafrost, field study, seep, engineered bubble plume

1. Introduction

1.1 Arctic Methane

Methane and Arctic climate change

On a century timescale, methane, CH_4, is the next most important anthropogenic greenhouse gas after carbon dioxide, CO_2 (Forster et al. 2007). However, on a decadal time scales comparable to its atmospheric lifetime, CH_4 is more important to the atmospheric radiative balance than CO_2 (IPCC, 2007; Fig 2.21). After nearly stabilizing, atmospheric CH_4 concentrations are increasing again, although the underlying reasons remain poorly understood (Nisbet et al., 2014). Despite likely increasing future natural emissions from global warming feedbacks (Rigby et al., 2008) and anthropogenic activities (Kirschke et al., 2013; Wunch et al., 2009), many current source estimates have large uncertainties with greater uncertainty in future trends, particularly for Arctic sources where global warming is the strongest, termed Arctic amplification (Graversen et al., 2008).

Arctic continental shelf sediment accumulates 5 times faster than other World's Oceans. Sedimentation for the Siberian Arctic shelf where the six Great Siberian Rivers outflow, has deposited organic carbon that approximately equals accumulations over the entire pelagic area of the World's Oceans. This leads to the thickest (up to 20 km) and most extensive sedimentary basin in the world, the "Arctic super carbon pool" (Gramberg et al., 1983).

Arctic permafrost CH_4 provides an important climate feedback, with Arctic warming releasing CH_4 sequestered in and under terrestrial (Friedlingstein et al., 2006; Lemke et al., 2007) and sub-sea permafrost, which is submerged terrestrial permafrost (Shakhova and Semiletov, 2009). The permafrost feedback drives methane bubble emissions escaping from the seabed to the atmosphere. Assessing these emissions is challenging due to the vast extent of the East Siberian Arctic Shelf (ESAS) seep field (Shakhova et al., 2014; Stubbs, 2010), the most extensive in the world, with sonar playing a role due to its remote sensing capability, critical for surveying larger areas.

Sonar has been used to survey concentrated seep area covering ~1000 m^2 in the North Sea (Schneider von Deimling et al., 2007; Schneider von Deimling et al., 2010; Wilson et al., 2015) and far more dispersed and weaker seepage in the Black Sea of ~2500 plume in an areas of ~20 km^2 (Greinert et al., 2010), and offshore Svalbard where a few hundred plumes were observed in an area of ~ 15 km^2 (Veloso et al., 2015). Significantly larger and stronger seepage in the COP marine hydrocarbon seep field, offshore

California have been mapped by sonar too. The COP seep field covers ~3 km^2 of active seabed in an 18 km^2 area releasing 10^5 m^3 CH_4 per day (Hornafius et al., 1999), and likely comprises many tens of thousands of plumes.

ESAS seepage is on a dramatically larger scale with ~30,000 plumes manually identified in just two transects (Shakhova et al., 2014; Stubbs, 2010). Seepage densities to ~3000 seep bubble plumes per km^2 were found transecting a single hotspot. Based on the hotspot size (18,400 km^2), an order of magnitude estimate suggests 60 million seep plumes in the hotspot alone. While a few minutes sonar survey can cover a localized site, e.g., the North Sea site, two sonar survey transects of the ESAS required a month.

1.2 Study motivation

Given the extent of the seepage area and the magnitude of current and potential future emissions, there is a critical need for new approaches to effectively, rapidly, and quantitatively survey large seepage areas. Video is inadequate to survey extensive or widely dispersed seepage, a task for which sonar (active acoustics) excels. This study demonstrates an improved approach to quantify seabed seepage using *in situ calibrated* sonar-derived bubble fluxes and its application in the Arctic.

Herein, we present *in situ* experiments that characterized bubble plume sonar return evolution as the bubble plumes rise. Both multiple beam echosounder (MBES) and single beam echosounder (SBES) data were collected. Engineered bubble plumes spanned a broad range of flow rates that spanned observed seepage bubble flows in the two study areas. The *in situ* experiments showed *non-negligible* effect from non-linear sonar interactions involving multiple bubbles. Thus, *in situ* experiments provided an *in situ* calibration of flux with respect to sonar return and height above source.

The calibration was applied to quantify *in situ* sonar observations of three natural seepage areas in the ESAS. Because the calibration bubble plumes and seep bubble plumes were different gases and from different depths, bubble dissolution rates are different – i.e., for the same seabed mean volume flux, the depth-window-averaged volume fluxes are different. We demonstrate a first correction attempt based on a numerical bubble-plume model for the two bubble flows (calibration and natural seepage). Unfortunately, bubble size distribution could not be measured with available equipment. Thus the model was initialized with a typical seep bubble-plume size-distribution.

1.2 The East Siberian Arctic Shelf

The Siberian Arctic Shelf subsea permafrost, CH_4 hydrate, and natural gas systems contains vast CH_4 deposits (Gautier et al., 2009; Gramberg et al., 1983; Romanovskii et al., 2005; Serreze et al., 2009; Shakhova et al., 2010a; Shakhova et al., 2010b; Shakhova and Semiletov, 2009) of which a large fraction is CH_4 hydrate deposits (Makogon et al., 2007; Soloviev et al., 1987). Subsea continental shelf reservoirs contain an estimated ~10,000 gigatonnes Gt (1 Gt=10^{15}g) of CH_4 hydrates (Dickens, 2003). This is vastly larger than the estimated ~400 Gt of CH_4 hydrates in terrestrial permafrost. The Arctic continental shelf comprises 25% of the entire area of the world's oceanic continental shelves (7 million km^2 of the ocean's area, 28.8 million km^2) and is estimated to contain 2,500 Gt of carbon as CH_4 hydrates. This is more than 3 times greater than the atmospheric carbon inventory and ~5000 times greater than the current atmospheric CH_4 reservoir (IPCC, 2007). Remobilization of even a small fraction of CH_4 in these deposits could trigger abrupt climate warming. For example, atmospheric release of just 0.5% of the CH_4 in Arctic shelf hydrates could cause abrupt climate change (Archer and Buffett, 2005).

The East Siberian Arctic Shelf (ESAS) is the world's largest and shallowest shelf (covering 2.1x10^6 km^2) containing the largest area of submerged permafrost by far (Shakhova et al., 2010a; Shakhova et al., 2010b). The ESAS is a seaward extension of the Siberian tundra that was flooded during the Holocene transgression, 7-15 kyr ago (Romanovskii et al., 2005). The ESAS comprises ~25% of the Arctic continental shelf and contains over 80% of global subsea permafrost and shallow hydrate deposits, estimated at ~1400 Gt carbon (Shakhova et al., 2010a). This reservoir includes the ESAS hydrate deposits, estimated at ∼540 Gt of CH_4 with an additional 2/3 (∼360 Gt) trapped below as free gas (Gramberg et al., 1983; Soloviev et al., 1987). The ESAS is a sibling to Siberian terrestrial permafrost that was submerged and is expected to contain similar permafrost organic carbon deposits to terrestrial. This implies a further 500 Gt organic carbon within an ~25-m thick permafrost layer. Thus, estimated ESAS carbon stores are comparable to the Arctic soil carbon pool, which includes tundra and taiga (~1000 Gt C) and coastal permafrost (~400 Gt C) (Tarnocai et al., 2009).

Permafrost Degradation

The ESAS subsea permafrost is changing in response to glacial/interglacial Arctic warming (~7°C) and warming from the overlying seawater (~10°C) since inundation in the early Holocene, with additional ESAS seawater warming in recent decades (Biastoch et al., 2011; Semiletov et al., 2013; Semiletov et al., 2012; Shakhova et al., 2014). The Siberian rivers transport additional heat arises to the Arctic shelf from the results of terrestrial ecosystem responses to global warming. This includes the degradation of terrestrial permafrost and increased river runoff, which warms shelf waters. In turn, this warm runoff drives a downward heat flux to shelf sediments and sub-sea permafrost (Shakhova and Semiletov, 2007; Shakhova et al., 2014). Also, there is the potential for abrupt CH_4 release on the ESAS and its continental slope related to temperature destabilization of shallow Arctic hydrates, whose extent is highly sensitive to temperature (Dickens, 2003).

Subsea permafrost is an impermeable lid (where continuous) preventing the upward migration of CH_4 and other geological fluids, hence the great concern for its degradation allowing release of sequestered CH_4 to the shallow ocean and then atmosphere. Both onshore and offshore Arctic permafrost degrade from thawing in two directions (Osterkamp, 2010; Shakhova and Semiletov, 2009). It can thaw from the top downward, in which the active layer expands downward creating taliks (bodies of thawed permafrost). Permafrost also can degrade from the bottom up as a result of geothermal heat flux, where heat from the Earth's interior flows upward, thawing frozen sediments from below. The latter only has a significant effect for submerged offshore permafrost (Romanovskii et al., 2005), because high Arctic terrestrial permafrost is thick and continuous allowing its bottom to absorb upward heat flows far better than offshore permafrost. For example, an offshore permafrost sediment core (obtained by authors' team from the fast ice in April 2011 to 57 m below the Laptev sea floor) was unfrozen and 8-12°C warmer than a core recovered from the Lena Delta' borehole (Shakhova et al., 2014). These observations change the view of the vulnerability of the large sub-sea permafrost carbon reservoir on the ESAS - the permafrost lid is clearly perforated, with all year round CH4 emissions to the atmosphere from the sedimentary reservoir, which is no longer safely sequestered (Shakhova et al., 2010a; Shakhova et al., 2015). IN contrast, CH_4 emission from the thawing soil is gradual and seasonal.

Recent studies indicate four subsea permafrost degradation mechanisms provide geologic control of the thermal state of subsea permafrost and also hydrate stability. The most important, which operates on long (millennia) timescales, is the increasing temperatures of the overlying bottom seawater and the duration of its interaction with the permafrost both by heat transfer and salinization (Shakhova et al., 2014; Shakhova et al., 2015; Soloviev et al., 1987). A third process that provides geologic control arises from heating from large Siberian rivers which drives bottom water warming and is proposed to control the distribution of open taliks in coastal ESAS waters (Shakhova et al., 2014). Finally, the high geothermal heat flow in rift zones induces fractures that provide geologic control (Drachev et al., 2003; Nicolsky et al., 2012). In addition, areas of high heat flow would include relic–thaw lakes and river-valleys that were submerged during the Holocene inundation, but still drive modern permafrost degradation (Nicolsky and Shakhova, 2010; Nicolsky et al., 2012; Shakhova and Semiletov, 2009).

Subsea permafrost degradation is greatest in the outer shelf waters (deeper than 50 m), where the submergence at the beginning of Holocene, ~10-15 thousands years ago, occurred first. As a result, current models predict discontinuous and mostly degraded permafrost in the outer Laptev Sea (Bauch et al., 2001). The formation and growth of subsea thaw lakes also likely is greater where riverine heat inputs combines synergistically with longer permafrost submergence (Hölemann et al., 2011; Shakhova and

Semiletov, 2007; Shakhova et al., 2014). This leads to an evolution of taliks, which provide effective gas migration pathways to the seabed in the shallow waters of the ESAS (Nicolsky and Shakhova, 2010; Nicolsky et al., 2012; Shakhova et al., 2009). Increasing river outflow also affects ocean temperatures by introducing colored dissolved organic matter, which concentrates solar radiation absorption into near surface waters, accelerating ocean warming, freshening, and acidification (Pugach et al., 2015; Semiletov et al., 2016; Semiletov et al., 2013).

Geologic heat flow is strong in the Laptev Sea (85-117 m W m^{-2}) where active seafloor spreading is converting into continental rifting. In fact, the northern Laptev Sea is one of the few places where active oceanic spreading approaches a continental margin (Drachev et al., 2003) and correlates with the "hot" area crossed by the Ust' Lensky Rift and Khatanga-Lomonosov Fracture (Drachev et al., 2003; Nicolsky et al., 2012). Evidence for this rifting is provided by hydrothermal fauna remnants documented around grabens (dropped blocks between faults) in the up-slope area that typically occur along oceanic divergent axes (Drachev et al., 2003). Grabens in the ESAS often are linear structures that correlate spatially with paleo-river valleys.

Migration from submerged ESAS permafrost to the seabed feeds a vast marine seep field entirely in shallow waters, whose emissions contribute directly to the atmospheric budget (Shakhova et al., 2014). At-sea observations show dissolved CH_4 supersaturation with respect to the atmosphere for >80% of ESAS bottom waters and >50% of surface waters (Shakhova et al., 2010a; Shakhova et al., 2010b). This seepage is almost entirely ancient CH_4 – modern CH_4 production from old organic carbon contributes negligibly based on recent microbiological studies (2011-2012) in ESAS surface and long-sediment cores (V. Samarkin, unpublished data). Indeed, in the ESAS, sediment organic carbon content varies by a factor of ~4, whereas ebullition CH_4 fluxes vary by orders of magnitude (Shakhova et al., 2015).

1.3. Marine seepage fate and bubble processes

Marine seepage is a global phenomena where CH_4 and other trace components escape as bubbles from the seabed and rise towards the sea surface (Judd and Hovland, 2007), dissolving and depositing CH_4 in the water column while transporting their remaining contents to the sea surface – if they do not dissolve subsurface (Leifer and Patro, 2002).

To address the difference in seep and calibration gases, a numerical bubble propagation model was used to explore the relative dissolution rates for the two types of bubble plumes. The bubble model is described elsewhere (Leifer et al., 2006; Leifer et al., 2015; Rehder et al., 2009). The model solves the coupled differential equations describing bubble molar content (Eqn. 1), size (Eqn. 2), pressure, and rise for each bubble size class in a bubble plume. These two equations are presented below as they describe how sonar observations of bubble volume (size) relate to bubble mass (molar content).

Bubble dissolution or gas flux (F_i) for each gas species i is the change in bubble molar content (n_i) driven by the concentration difference (ΔC_i) between the bubble and the surrounding water,

$$F_i = \frac{\partial n_i}{\partial t} = k_{Bi} A(\Delta C_i) = k_{Bi} A(C_i - H_i P_i) \qquad (1)$$

where k_B is the individual bubble gas transfer rate and depends on the gas diffusivity and equivalent spherical radius, r_e, A is the bubble surface area, H is the Henry's Law equilibrium, and P is the bubble partial pressure. Seep gases, like methane largely outflow (positive F) while air gases inflow (negative F)

The flux, F_i, depends on depth and bubble size (Leifer and Patro, 2002). Bubble size affects the bubble's fate because k_B depends on the gas diffusivity and equivalent spherical radius, r_e, and A clearly depends on r_e. Deeper bubbles with the same size contain greater mass, which allows them to survive longer. Seep bubbles are seldom isolated (Leifer, 2010), thus plume processes are important, including the upwelling flow which depends on the total plume volume flux (Leifer et al., 2009; Leifer et al., 2006). Another plume process is enhanced aqueous concentrations relative to the surrounding water, which enhances bubble survival (Leifer et al., 2006).

$$\frac{\partial r_e}{\partial t} = \left\{ \mathbf{R}T \frac{\partial n}{\partial t} - \frac{4\pi r_e^{\,3}}{3} \rho_W g \frac{\partial z}{\partial t} \right\} \left\{ 4\pi r^2 \left(P_A - \rho_W g z + \frac{2\alpha}{r_e} \right) - \frac{4\pi r^3}{3} \frac{2\alpha}{r_e^2} \right\}^{-1} \qquad (2)$$

were $\mathbf{R}$ is the universal gas constant, T is temperature, and n is the molar sum of all gases. This first term describes how the flux changes the bubble molar content and hence the change in bubble size with time (t). The second term describes how changes in hydrostatic pressure as the bubble rises (i.e., depth (z) decreases) affects bubble size, and depends on water density (ρ_W) and gravity (g). The denominator also includes the effect of surface tension (α) on pressure – higher pressure implies a smaller bubble.

The ultimate fate of dissolved seep CH_4 depends most strongly on its deposition depth (Leifer and Patro, 2002) with CH_4 below the Winter Wave Mixed Layer (WWML) largely being oxidized microbially (Rehder et al., 1999). In the shallow Coal Oil Point (COP) seep field, most of the CH_4 reaches the atmosphere directly (Clark et al., 2005) from mixing in the near field (Clark et al., 2000) and in the far (down-current) field when winds strengthen as typical occurs diurnally in coastal California. Even for deepsea seepage (to ~1 km), field studies show seep bubble-plume CH_4 transport to the upper water-column and atmosphere (MacDonald, 2011; Solomon et al., 2009) due to plume processes and hydrate skin phenomena (Rehder et al., 2009; Warzinski et al., 2014). Note, a significant fraction of deepsea seabed CH_4 emissions are deposited below the WWML where they are dissolved and oxidized microbially. In the shallow ESAS, virtually all the seabed CH_4 (dissolved and gaseous) is emitted in the WWML and escapes to the atmosphere directly or from frequent storms (Shakhova et al., 2014). However, even CH_4 dissolved below the WWML is less likely to be oxidized than in non-Arctic waters column because CH_4 oxidation rates are very low, 300-1000 days (Shakhova et al., 2015) allowing release to the atmosphere of some of this deeper aqueous inventory during storms and fall-winter convection (Shakhova et al., 2010a; Shakhova et al., 2014).

1.3 Sonar seep observations

Sonar is highly effective at seep emission mapping; however interpretation challenges exist even for qualitative assessment of relative emission strength. For single beam echosounders (SBES), there is geometric uncertainty (Leifer et al., 2010) – the plume's angular location is unknown; a problem resolved by multibeam echosounders (MBES). Additionally, sonar (SBES or MBES) loses fidelity from multiple plumes in close proximity (Schneider von Deimling et al., 2011; Wilson et al., 2015) where the sonar returns along multiple pathways, creating ghosts, shadow noise, off-beam returns, scattering loss, and other artifacts (Wilson et al., 2015). Note, if bubble spatial densities are sufficiently high for artifacts to occur between plumes, then they are sufficiently high to produce artifacts within plumes between individual bubbles. For very high flux bubble plumes, the sonar return signal can be largely or even completely lost (Leifer et al., 2010). Also, the vessel acoustic environment can be challenging from acoustic and electrical noise, while, signal loss from scattering also can occur from suspended sediment and biota, often in layers.

Although seemingly straightforward, there are many challenges to quantitative derivation of bubble emission flux from sonar return, which at its basis relates to the interaction of sound with a bubble. For a single spherical bubble the relationship has long been known, with resonance given by the Minnaert (1933) equation:

$$f_o = \frac{1}{2\pi r_e}\left(\frac{3\gamma P}{\rho}\right)^{1/2} \tag{3}$$

where f_o is the resonance (or Minnaert) frequency, γ is the resonance (or Minnaert) frequency, P is internal bubble gas pressure, and ρ is pressure, and for non-spherical bubbles (r_e > 150 μm) an eccentricity correction is needed to account for the angle between the bubble axes and the sound wavefront. Bubble eccentricities vary from 1.0 for spherical bubbles to 2 or greater for $r_e > 3500$ µm (Clift et al., 1978).

For a single spherical bubble, the back-scattering cross section (σ_B) near f_o is (Weber et al., 2010):

$$\sigma_B = \frac{r_e^2}{\left[\left(\frac{f_o}{f}\right)^2 - 1\right]^2 + \delta^2} \tag{4}$$

where f is frequency and δ is the damping term that can be approximated as $\delta \sim 0.03 f^{0.3}$ with f in kHz.

From, here, integrating over the bubble emission size distribution ($\Phi(r_e)$, which is the number of bubbles in a r_e bin, passing through the measurement plane, combined with the bubble vertical velocity ($V_Z(r_e)$), which is a function of r_e over the measurement volume yields the total plume cross-section if bubbles are acoustically non-interactive and scattering is isotropic.

In most seep bubble plumes, the close proximity between bubbles creates bubble-bubble acoustic interactions through acoustic coupling and/or multiple scattering. Acoustic coupling occurs for bubbles within 10-20 bubble radii of each other, i.e., a few centimeters, leading to a frequency shift (Leifer and Tang, 2006). Because sonar is spectrally selective, frequency shifts from acoustic coupling can decrease the sonar return signal. In most seep bubble plumes, acoustic coupling should be small except very near the seabed where bubbles still rise in close proximity, or where bubbles rise in dense clumps. In the latter case, smaller bubbles often draft larger bubbles and remain in close proximity (Tsuchiya et al., 1996).

Multiple scattering occurs when the sound scattered from one bubble interacts and scatters from a second bubble back in the direction of the sonar receiver. The impact of multiple scattering on sonar return depends on the spatial variations of the bubble size distribution within the plume, which is asymmetric from currents, and evolves as the bubble plumes rises. Additional complexity arises in that multiple scattering is not radially symmetric with plume axis, due to compressibility (i.e., gas volume fraction) varying with azimuthal angle, and because bubbles are eccentric. Artifacts, like ghosting between plumes (not side lobe sonar return), provide evidence of significant multiple scattering on length scales larger than the plume diameter. Note, such artifacts inside the plume cannot be spatially segregated as they also occur inside the plume.

2. Methodology

2.1. Field Study areas

This study reports on the use of *in situ* engineered plumes for calibration of sonar return to derive quantitative flux rates using a MBES which was deployed in the Coal Oil Point (COP) seep field, offshore California in the northern Santa Barbara Channel,in the Kara Sea, and in the ESAS. We present only a small fraction of collected Kara Sea and ESAS data, which were cleared for publication.

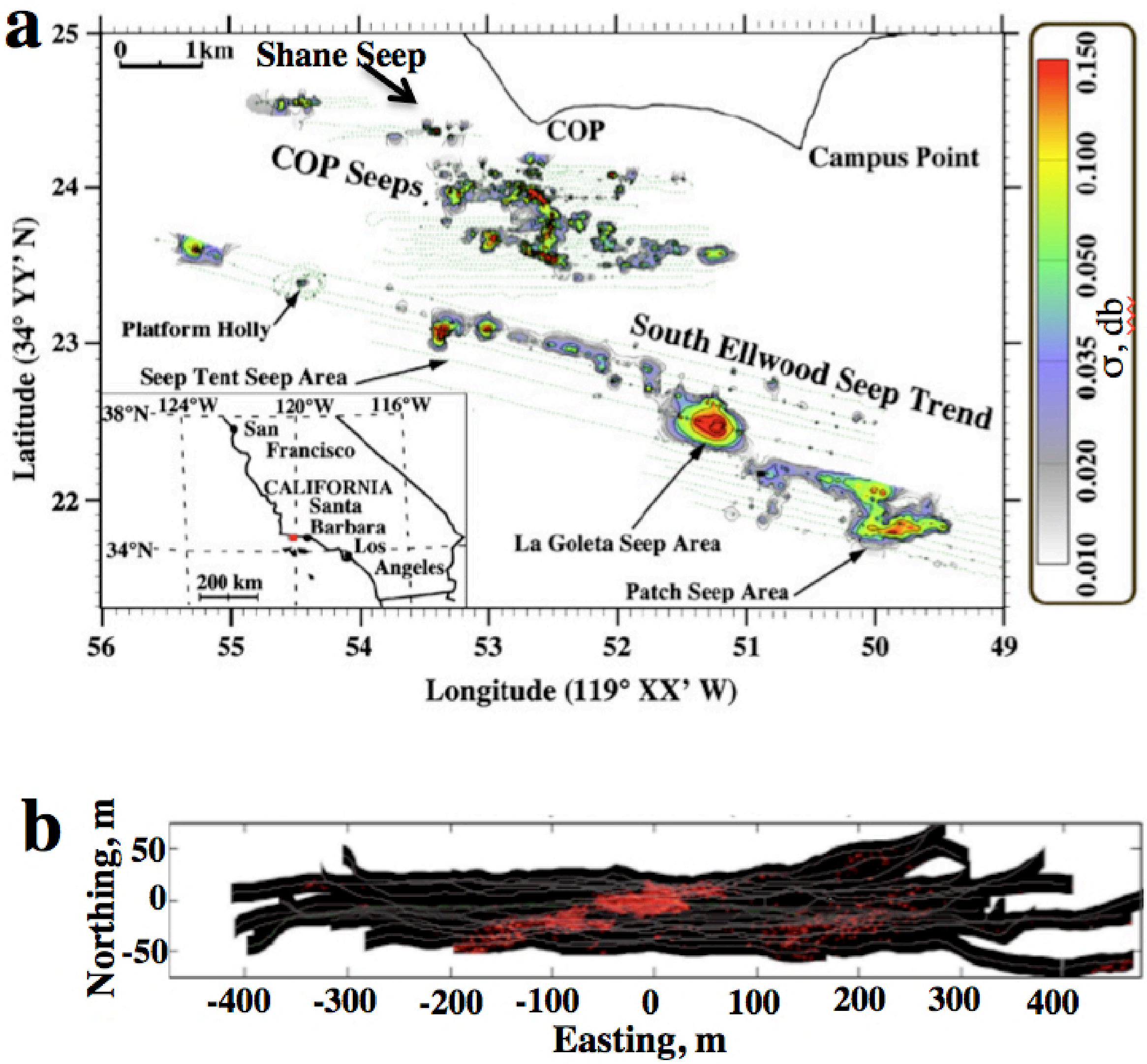

Figure 1. a. Coal Oil Point (COP) seep field map, showing the Shane Seep area of the scoping study. Sonar data from 2005. Adapted from Leifer et al. (2010). **b.** Shane Seep multibeam sonar survey map of seep detection (2-m depth window at a seabed-following height of 4 m). MBES data collected in 2009.

2.1.1. Coal Oil Point seep field

A precursor study was conducted in the COP seep field prior to the Arctic field experiment to demonstrate 4D seep monitoring by a scanning MBES (**Fig. 1**). The rotator-lander was deployed ~15 m from the center of Shane Seep, which covers an area of ~10^4 m^2 in ~20-m water depth and comprises on the order of 1000 individual vents or bubble plumes (Fig. 1B). The lander included a MBES (DeltaT, Imagenex, Vancouver, Canada) and compass (Ocean Server, MA) on an underwater rotator (Sidus Solutions, CA) with azimuthal rotation of up to 270° angle range. The sonar produced a 260 kHz, vertically-oriented 128-beam fan spanning 120°, tilted upwards to reduce seabed backscatter. Two *in situ* calibration air bubble flows were deployed ~8 m from the lander at azimuthal angles beyond the active seepage area and were traversed during each sonar rotation cycle. Two rotameters measured regulated airflows from an onboard compressor to these two bubble plumes .

2.1.2 Arctic Field Campaign

Field data were obtained during an expedition onboard the research vessel R/V *Victor Buynitsky* from 2 Sept. to 3 Oct. 2012 (**Figs. 2 and 3**). The R/V *Victor Buynitsky sailed* from Murmansk to the Laptev Sea and the adjacent portion of the ESAS. The expedition's overarching goal was to improve understanding of the current scale of ESAS CH_4 emissions in order to develop a conceptual model of CH_4 propagation from the seabed to the atmosphere, including assessing source strengths and their dynamics.

The calibration experiments were conducted in a region of no natural seepage and almost flat seafloor in the Kara Sea (**Fig. 3**) to reduce or eliminate off-beam acoustic seabed scattering. Water depths were 45-m under favorable weather: calm sea with wind speed 1-3 m s^{-1} and wave height of 0.2-0.5 m with no significant waves (0 to 1 ball). Column profile temperature and salinity data were obtained by a conductivity temperature depth (SBE19+, Seabird, USA). Weather for the seep sonar survey was typical (3-4 storm events with wind speed >10 m s^{-1}).

The vessel was anchored during the engineered sonar bubble plume experiments. Engineered bubble plumes were made from nitrogen supplied by a pressure tank on the vessel foredeck. A 70-m long, 12-mm diameter, 6-mm wall thickness, air supply tubing was attached by a Kevlar rope to a heavy metal weight (~30 kg) that ballasted against buoyancy of air in the tubing and drag from currents. The supply tube was deployed to 40-m depth in water of ~45-m depth (**Supp. Fig. S3**) and the rising bubble plume was observed with MBES and SBES. The sonars were located near each other so that their beam coverage overlapped with the center beam focused on the end of the bubble stream. Bubbles were produced from a 4-mm diameter copper nozzle attached at the end of the air supply tube.

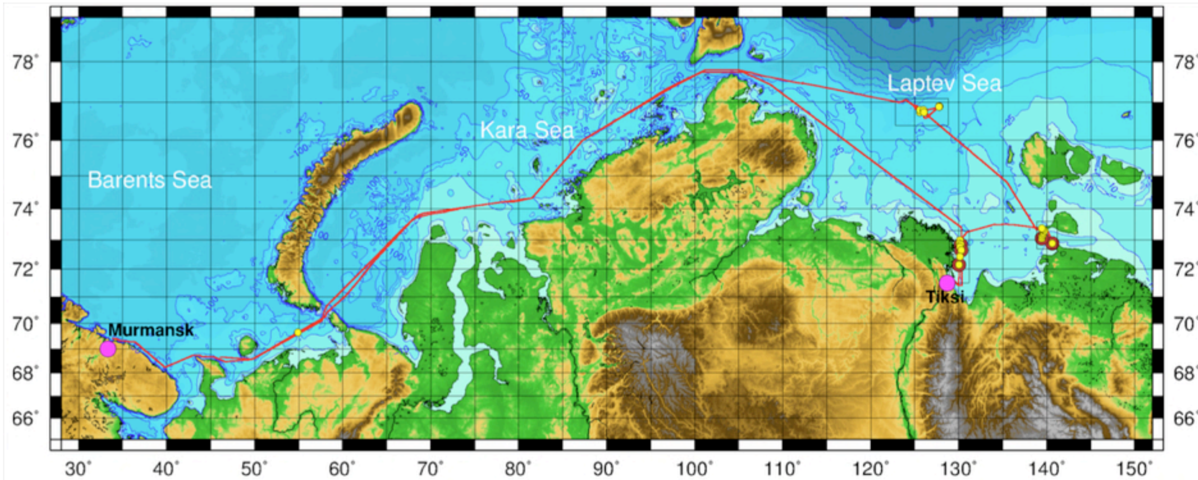

Figure 2. Map for R/V *Victor Buynitsky* cruise, 2012.

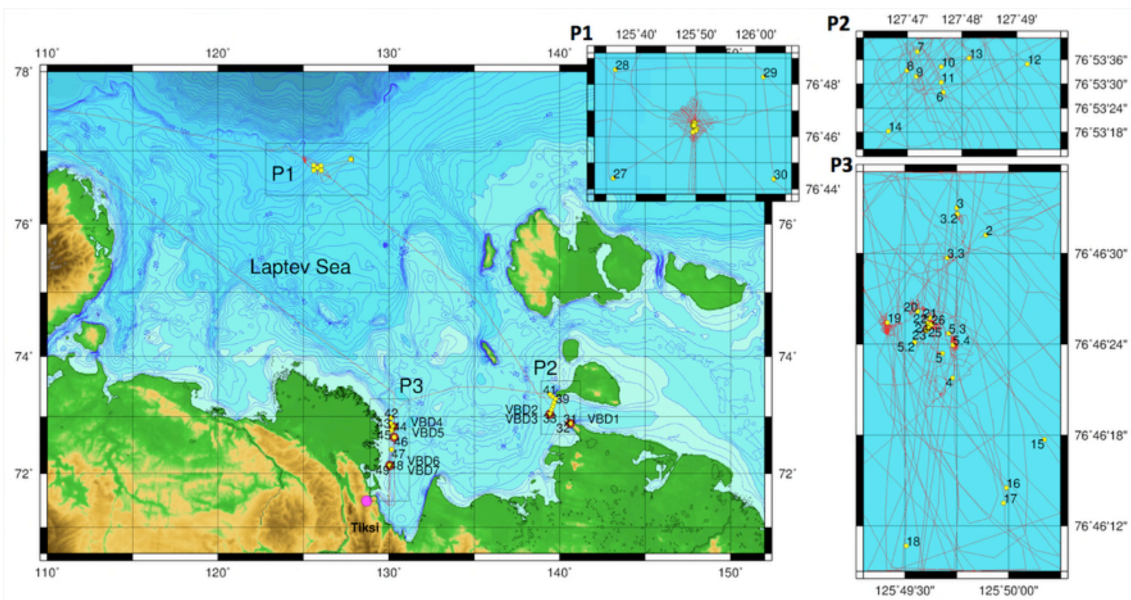

Figure 3. Locations of oceanographic stations for RV *Victor Buynitsky* cruise, 2012, marked by yellow circles. Polygons of major focus areas are marked as P1 (northern Laptev Sea), P2 (east Lena Delta) and P3 (Dmitry Laptev Strait), shown in insets. Ship tracks accompanied by CTD measurements (and geophysical survey) performed in the P1 are shown as red lines.

Gas flow was controlled using standard flow meters, one port of which was connected to a PVC tube and another was connected to a 2-way valve, the second port of which was connected to the gas tank through the gas manifold. The manifold consisted of a high-pressure sensor of the tank pressure and a low-pressure sensor for the out-coming pressure (5.5 bar). We used temperature-compensated differential pressure sensors with a manufacturer-specified range of ±1 psi (equivalent to ±70 cm of water). The sensor has manufacturer-specified accuracy and stability of ±0.5% FSD (full scale deflection over the operating pressure range of the sensor over 1 yr, between 0 and 50°C) and repeatability errors of ±0.25% FSD. For the study, the gas flow was varied from 0.5 to 150 L min^{-1} at 5.5 bar (equals the bubble outlet hydrostatic pressure). For each experiment, the gas flow was allowed to stabilize and then sonar data were recorded for ~10 minutes.

The MBES was the same used in the Coal Oil Point seep field. The SBES was a SIMRAD EK15 SW 1.0.0 echosounder (www.simrad.com) at 200 kHz, with a 1 ms pulse duration at 10 Hz, 26° beam width, and built-in calibration system. Sonar data including seep bubble plumes were recorded at an average survey speed of 4-6 knots. Sonar backscatter was calibrated using acoustic targets (SIMRAD, Denmark). Initial data visualization and processing used EchoView and Sonar5 software (SIMRAD), for the EK15.

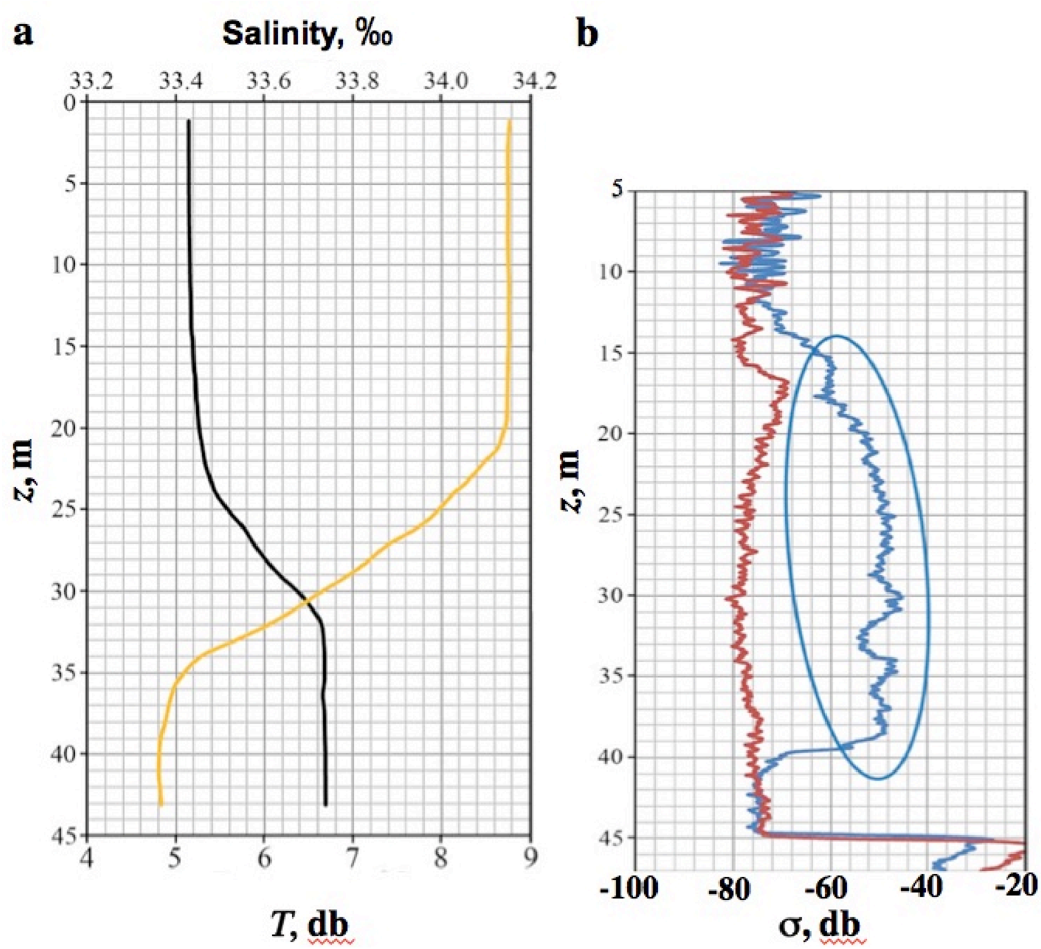

Figure 4. a. Salinity and temperature (T) with respect to depth (z) during engineered bubble plume experiments. **b.** Single beam echosounder sonar return integrated across the plume (σ) with z for no bubble plume (red) and a bubble plume (blue), bubble plume σ circled.

Bubbles have high density-contrast with water and thus are strong sonar targets that can be distinguished easily from the background (**Fig. 4b**). For the engineered bubble plume experiments, the wave-mixed layer (WML) extended to ~35 m depth with upper water warmer by ~3.5°C than deeper water (**Fig. 4a**).

Sonar data analysis and visualization was performed with custom MatLab routines (Mathworks, Mass.) that first geo-rectified each ping and then assembled the data for each experimental run into a 3-dimensional array of depth (z) transverse distance (x) and along track distance (y) or time (t) if stationary.

2. 2 Seep and engineered bubble plume modeling

A volumetric correction factor was developed to account for differences in the seep and calibration gases plumes based on the numerical bubble propagation model. Unfortunately, bubble size distributions were not measured, thus a typical minor bubble size distribution from the literature was used. Implications of these simplifying assumptions are discussed in Section 4.4.

Currently, natural seepage bubble-plume size distributions (Φ) only have been measured directly by video (Leifer, 2010; Römer et al., 2012; Sahling et al., 2009) and passive acoustics with the latter only demonstrated for low-emission-rate bubble plumes where the acoustic signature of the individual bubbles can be identified (Leifer and Tang, 2006; Maksimov et al., 2016).

Natural seepage bubbles largely fall within a narrow size range. Specifically, based on a review of 39 bubble-plume size distributions (the most comprehensive published dataset to date), Leifer (2010) found that the vast majority of reported seep bubble plumes could be classified in two primary categories, termed major and minor, with the latter most common, a characterization found in other studies, reviewed in Leifer (2010). Φ for minor bubble plumes are well described by a Gaussian function and comprised of bubbles largely in a narrow size range, $1000 < r_e < 4000$ µm, where r_e is the equivalent spherical radius. Major bubble plumes generally escape from higher flow vents as a fragmenting gas jet with a power law size distribution (Leifer and Culling, 2010). Most major bubble plumes are small; however most of the plume volume is transported by the largest bubbles, up to $r_e \sim 1$ cm (Leifer et al., 2015).

The model was initialized with a typical (Leifer, 2010) minor Φ (**Fig. 5a**) for either methane or nitrogen bubbles, dissolved air gases at equilibrium in the water column, the observed CTD profile (**Fig. 5b**), and a 10 cm s^{-1} upwelling flow (V_Z). V_Z is an average value that is too low for the highest calibration flow and too high for the lowest (Leifer, 2010).

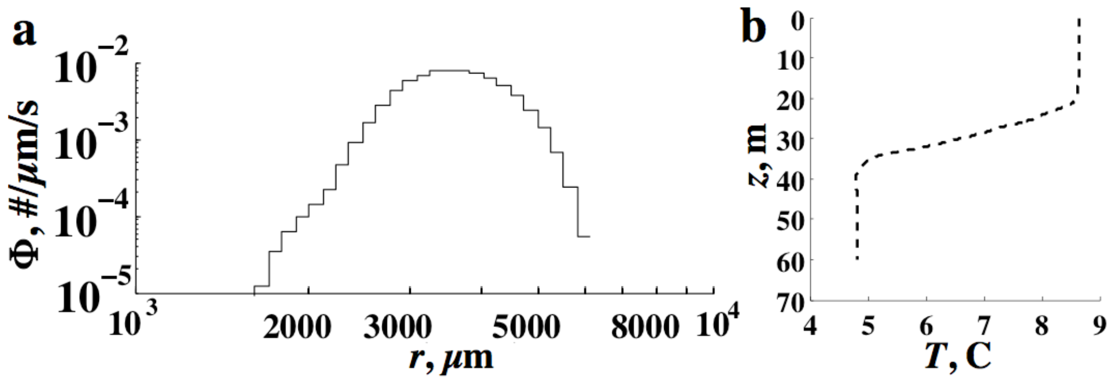

Figure 5. a. Minor bubble plume size distribution (Φ) with respect to equivalent spherical radius (*r*) used to initialize the bubble model. **b.** Measured temperature (*T*)-depth (*z*) profile used in model.

3. Results

3.1. Engineered bubble plumes

Sonar return (σ) for the two calibration plumes (**Fig. 6**) were thresholded above background (bubble-free water) and integrated for each beam during rotation across each calibration plume. The thresholded σ in a depth window then was fit with a linear polynomial of the log of the integrated sonar return over the plume versus height, *h*. As the bubble plume rose, σ increased – i.e., σ(*h*) was not constant (**Fig. 6**). Note, the change in volume for air bubbles over such short rise heights is negligible. This is evidence of bubble-bubble acoustic interaction decreasing as the bubbles rise and spread from turbulence (acoustic interactions decrease towards zero as the inter-bubble distances increases to large distances). Note, this data was not calibrated, and thus cannot be directly compared to the data in the East Siberian Arctic; it is presented to show the depth trends.

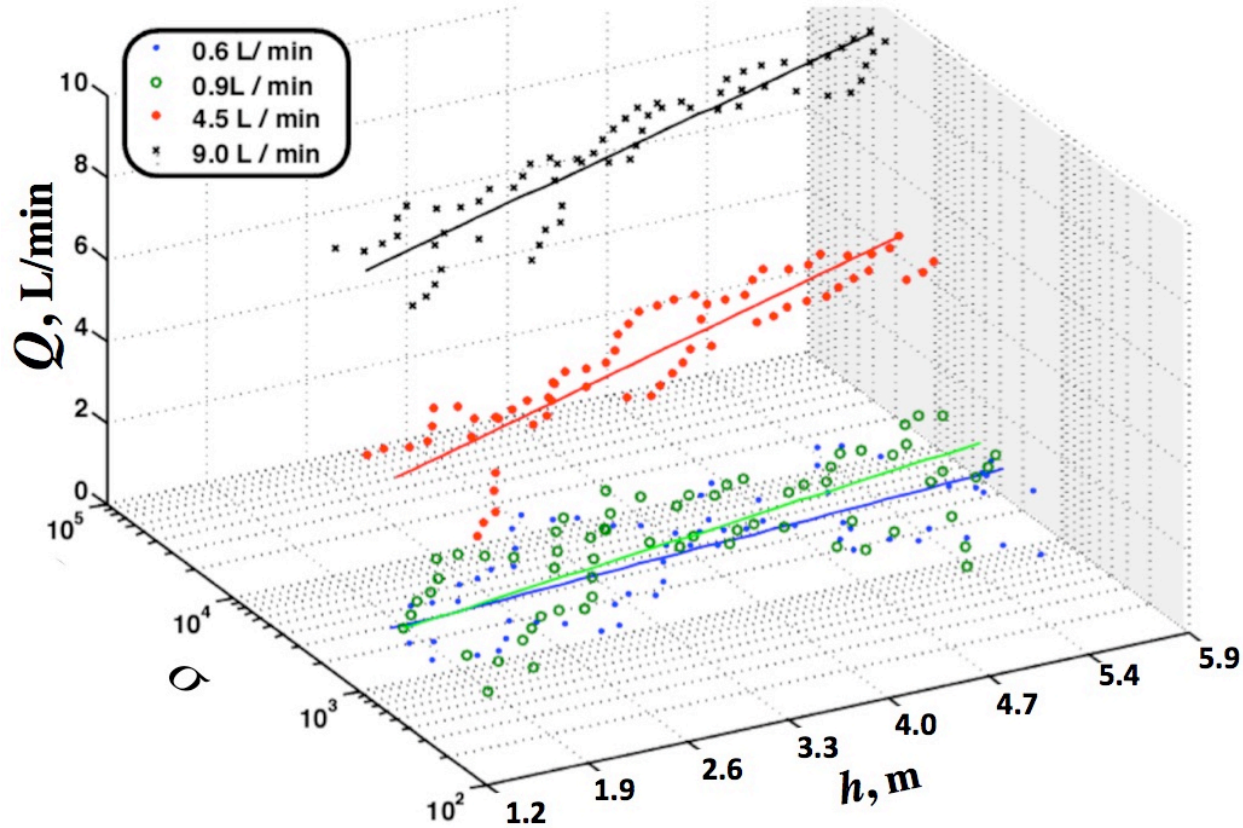

Figure 6. Field sonar data from the Coal Oil Point seep field for air bubbles in 22-m deep water. Sonar return counts integrated across the plume, σ, versus airflow, *Q*, and height above seabed, *h*, for four airflows and least-squares linear-regression fits to log(σ) versus *h*.

There is significant geometric uncertainty in SBES data, which is evident in the overlap in time of sonar returns for the calibration bubble plume (**Fig. 7**). This overlap results from current advection of the plume orthogonal to the page. MBES addresses this SBES deficiency. For example, the SBES sonar loses the bubble plumes once they have rose into the WML, where currents often shift, but the MBES continues to observe them to 13-m depth, slightly below the draft of the R/V *Viktor Buynitsky*.

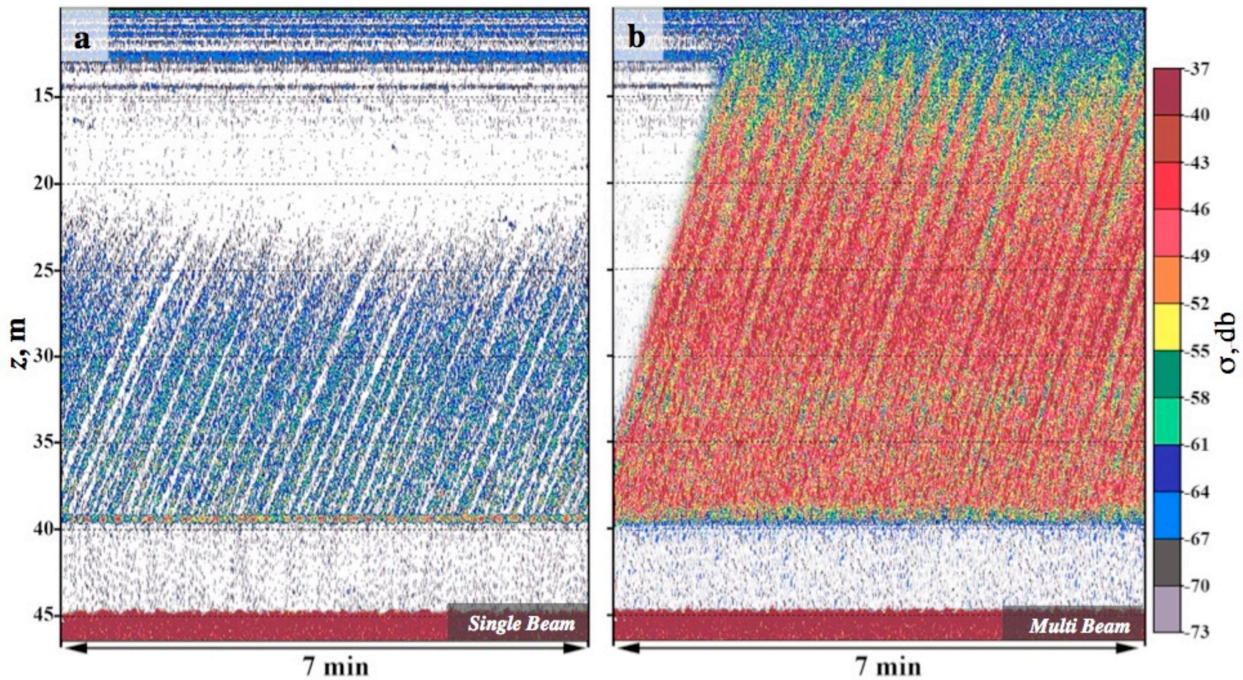

Figure 7. Plume-integrated sonar return, slume-icalibration bubble plume from 40-m depth, *z*, experiment conducted for **a.** 0.042 L/min and **b.** 1.1 L/min at 5.5 bar for the single beam sonar.

The most common sonar return ping element is noise, which was isolated from the bubble-plume signal based on setting a threshold from the sonar return probability distribution function ($\Psi(\sigma)$) at approximately – 80 db (**Fig. 8a**). $\Psi(\sigma)$ weaker than -70 db is clearly distinct from the stronger, but less common (lower Ψ), bubble $\Psi(\sigma)$. Based on inspection of $\Psi(\sigma)$, a noise threshold value of -70 db was selected (**Fig. 8a**, arrow), which provided a 5-8 db transition between noise and bubbles. Obvious sonar artifacts, which can exhibit strong sonar return signatures, were masked by spatial segregation. Specifically, the plume center was identified at each depth and then filtered to ensure continuity with depth. Then, only samples within a specified horizontal distance from the plume centerline that tightly constrained the plume above the noise threshold were incorporated into the analysis.

For the engineered bubble plume experiments, plumes with volume flux (*Q*) from 0.019 to 1.1 L/s were created and observed by both SBES and MBES systems (**Fig. 8**). The contribution of bubble plume weak and strong sonar returns were investigated by their signature in $\Psi(\sigma)$. Specifically, $\Psi(\sigma)$ was modeled by a piece-wise least-squares, linear-regression analysis of $\Psi(\sigma) = a\sigma(z)^b$. This model then was compared to expected trends in plume evolution of a rising bubble plume. Fit parameters are shown in **Supp. Table S1**. Example data and fits for the 0.8 L/s plume shown in Figs. 9d-9f for three depth windows (all below the WML).

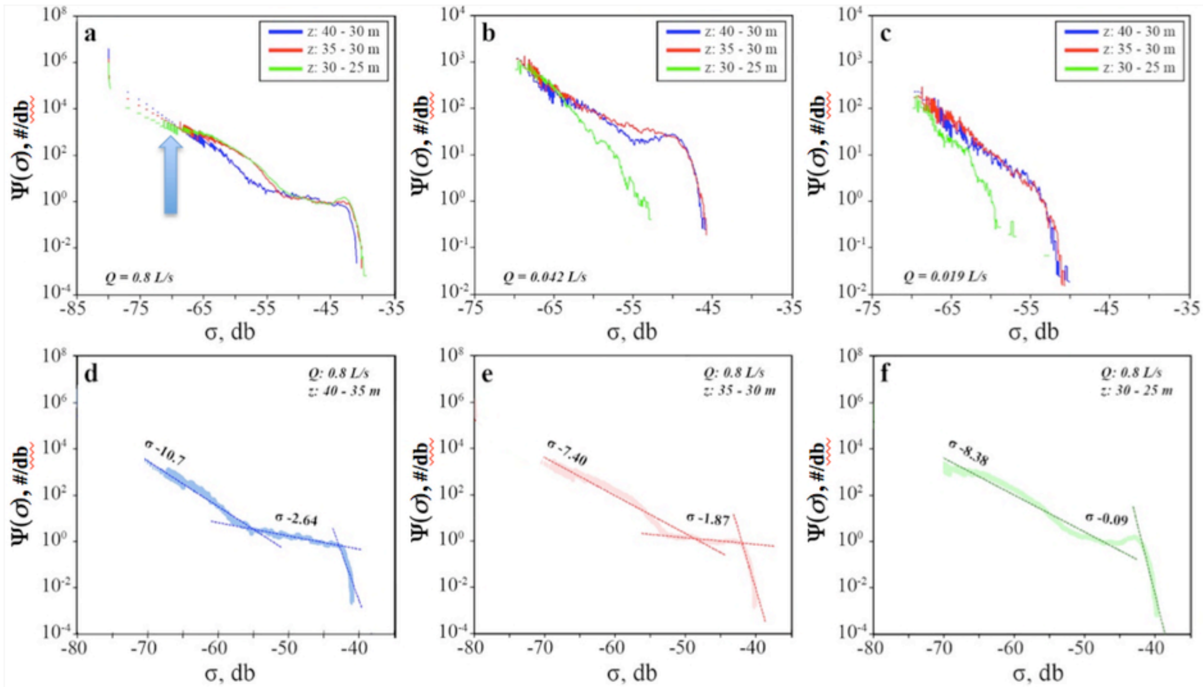

Figure 8. Plume-integrated sonar return (σ) occurrence probability distribution function (Ψ(σ)) normalized to sonar bin-width (sonar bins are logarithmically spaced) for **a.** full water-column for a flow, Q, of 0.8 L/s – unthrestholded for processed depth windows, z, arrow shows noise threshold. Ψ(σ) thresholded for **b.** Q = 0.042 L/s, **c.** 0.019 L/s and with linear fits for Q = 0.8 L/s for **d.** z = 35-40 m, **e.** 30-35 m, **f.** 25-30 m. Data key on figure. Fit parameters in **Supp. Table S1**.

For low and high flow, Ψ(σ) s exhibited distinctly different characteristics with Ψ(σ) for the intermediate-flow plume exhibiting characteristics of both low and high flows. A weak sonar return represents small bubbles, while strong returns may reflect large bubbles or it may reflect dense aggregations of small and/or large bubbles. As a bubble plume rises, the relative importance of small bubbles should increase as small bubbles disperse, spreading the weak sonar return over a larger volume. Ψ(σ) at the deepest depth for the weakest bubble plume exhibits a clear, two-part power law (**Fig. 8c**; **Supp. Table S1**) and remained constant as the bubble plume rose for the first 10 meters, then abruptly steepens in the next 5 meters, i.e., emphasizing the importance of smaller bubbles (b = -8, -7, -12 for weak σ for the 45-40, 40-35, 35-30 m depth windows, respectively). For the weaker bubble plumes (0.042 and 0.019 L/s, **Figs. 8b and 8c**, respectively), the strongest sonar returns disappear completely at the shallowest depth, consistent with bubble-plume dispersion and bubble dissolution.

Ψ(σ) is bi-modal for the deepest depth window for the highest-flow plume (**Fig. 8d**) with stronger returns more common relative to weaker returns than in the low flow plume (**Fig. 8c**) or than "predicted" by extrapolating the weak σ power law fit ($\sigma^{-10.7}$) to stronger σ (**Figs. 8d and 8f**, respectively). As this plume rose, Ψ(σ) for weak σ decreased in relative importance while Ψ(σ) for stronger σ remains constant – the power law exponent, b, for the intermediate depth (-7.4) was less steep than for the deeper (-10.7) and shallower (-8.4) depths. Thus, most of the evolution of Ψ(σ) is due to a spatial expansion of weaker σ, i.e., smaller bubbles, while the denser, strong σ bubbles remain relatively uniformly constrained with depth. The overall increase in σ with rise is the same character observed in the precursor study (**Fig. 6**), which featured strong plumes comparable to the strong plumes in **Figs. 8d-8f**.

Ψ(σ) for the intermediate flow plume (**Fig. 8b**) shares characteristics of both the high and low flow plume Ψ(σ), bi-modal at the deepest depth with a pronounced strong σ peak in Ψ(σ) (like the high flow plume) evolving into a dual power law as the plume rises – as for the low flow plume Ψ(σ). Thus, Ψ(σ) for the intermediate flow plume evolved through the patterns of the strong to weak flow plumes as it rose.

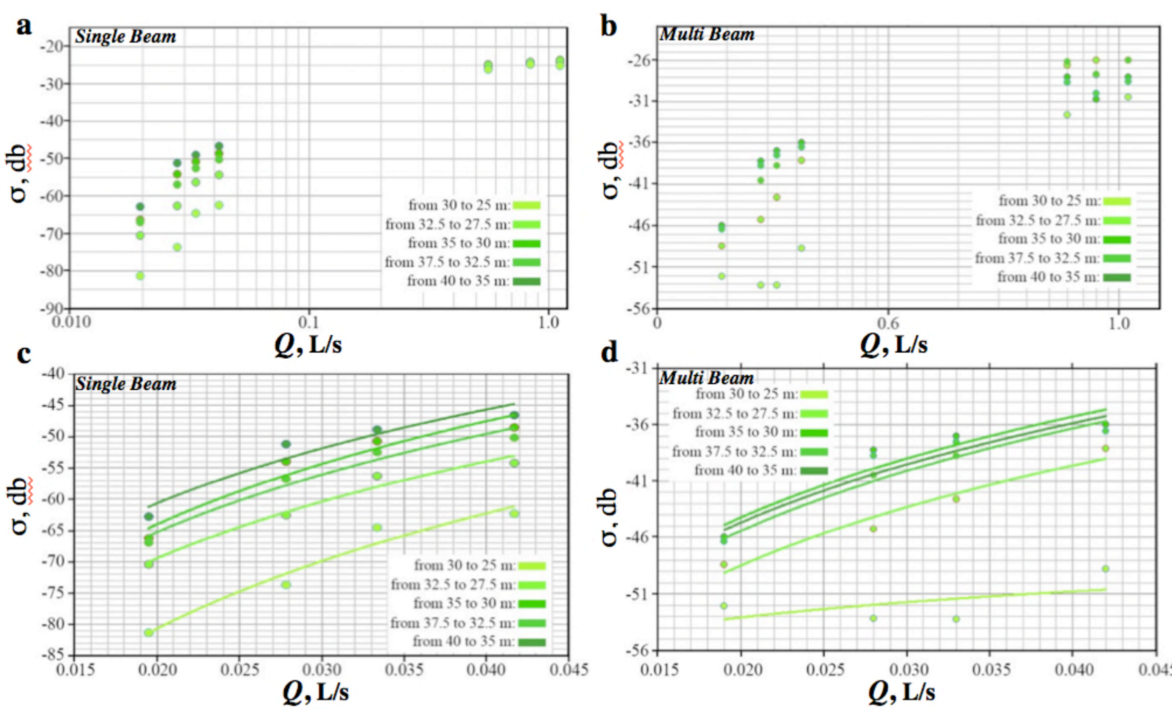

Figure 9. Sonar return, sonar return, yet iQ, calibration curves for the single-beam sonar for **a)** all Q, and **c)** low Q, and for the multibeam sonar for **b)** all Q and **d)** low Q. Fit parameters are shown in Supp. Table S2.

These are point source plumes that disperse as they rise, thus bubble-bubble acoustical interactions should decrease with height. With the exception of the strongest plume, plume rise decreases σ; however, for the strongest flow plume, rise initially increases σ, similar to the behavior in the precursor study (**Fig. 6**), which was for comparably high flows, albeit over depths much closer to the source. Example MBES data for these flows are presented in the **Supp. Figs. S1 and S2**.

Calibration curves of $\sigma(Q,z)$ were derived to account for the depth-evolving bubble-bubble acoustic interactions as the bubbles rose (**Fig. 9**). Specifically, σ above the noise threshold in the spatially-segregated boxes in each depth window is averaged over 7-minutes of sonar data for each flow to derive depth-dependent calibration curves of $\sigma(Q,z)$. The MBES and SBES calibration datasets show saturation at high flow, similar to Greinert and Nützel (2004), which is evidence of bubble-bubble acoustical interaction. For the high flow cases, this likely includes sonar shadowing of more distant bubbles by nearer bubbles (decreasing total return). At low flow, σ increases with increasing Q far faster than linear addition of the number of bubbles. For example, for a flow doubling (Q=0.02 to 0.04 L/min), σ should increase $20\log_{10}(2)$, or 6 db, yet increases are much larger.

The calibration curves show a depth dependency in σ for both SBES and MBES systems (**Fig. 9**). For low flow plumes, σ decreases with rise and is non-linear with Q. In contrast, for high flows, both SBES and MBES saturate or are near saturation although there is significantly more variability in the MBES data. Saturation occurs when increased Q has minimal to no increase in σ. Close inspection of the high-flow plume MBES data revealed undulations, which may have led to depth aliasing of σ in the 5-m depth windows. Although the high flow calibration plumes are relevant for major seep bubble plumes such as in COP seep field (Leifer, 2010); plumes in the ESAS study area were not this strong, and the strong calibration plumes are not discussed further. In contrast, the low flow calibration plumes are comparable to typical minor bubble plumes (Leifer, 2010) and span the range of natural seepage in the study area.

These *in situ* calibration curves were derived for application to seep bubble sonar survey data. Moreover, the calibration accounts for the vertical velocity of the bubbles, which includes buoyancy and upwelling flow. Application of the calibration curve should account for the depth difference between the seep study area and the calibration plumes (70 versus 40 m) and different composition –seep gas primarily is methane, while the calibration gas was nitrogen. Both these factors have non-negligible implications for the bubble dissolution rates of the two different plumes, which we make a first effort to address through numerical bubble simulations to account for differing dissolution rates and thus differing mean volume flux over the depth windows.

3.2. Bubble Dissolution Rates and Volume Flux

As noted, the seep gas and calibration gases were different as were the depth of the two bubble plumes. As a result of these differences the bubble plume evolves differently leading to different volume height profiles. Thus, a volumetric correction factor was developed based on the ratio of the volume height profiles between a calibration and a seep bubble plume (same bubble size distribution) based on numerical bubble propagation model simulations.

The numerical simulations show that for the first three, 5-meter depth windows, the depth-averaged total bubble plume volume ($<Q_z>$) increases (**Fig. 10b**) by 4.7%, 15%, and 29%, respectively. This growth occurs from decreasing hydrostatic pressure (primarily) and from oxygen inflow (secondarily), while it shrinks from nitrogen outflow. Growth indicates the balance favors against nitrogen outflow dominating.

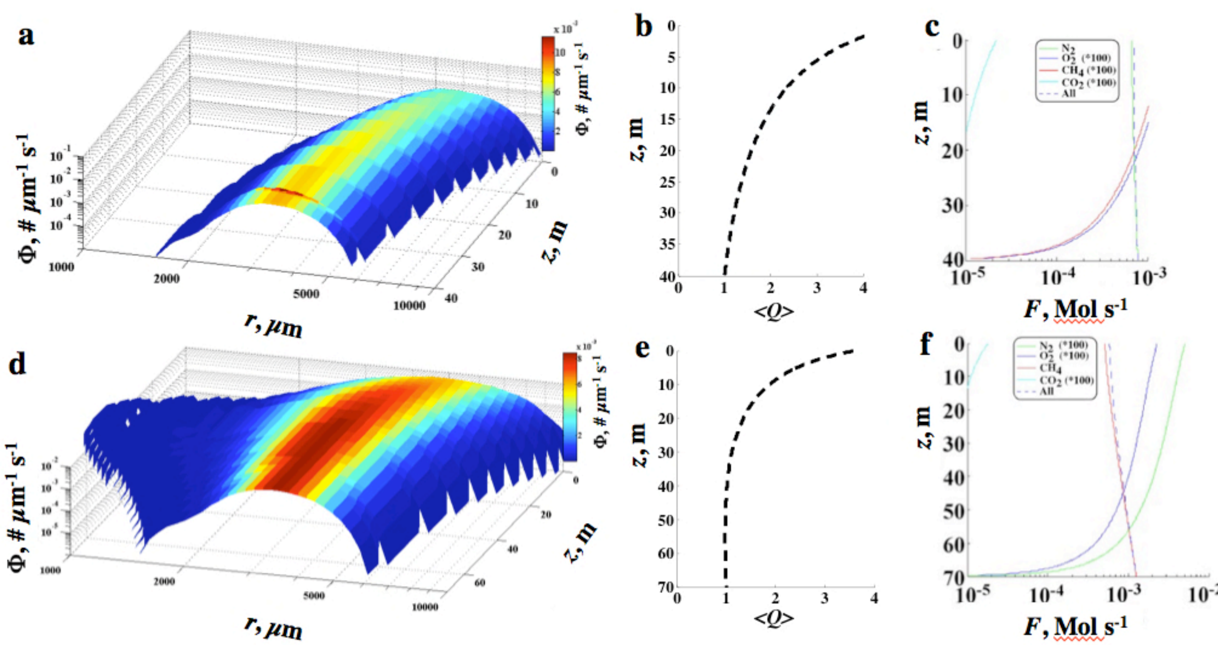

Figure 10. a Depth (z) evolution of the bubble plume size distribution (Φ) for a nitrogen minor plume (calibration) from 40 m and **d** for a CH_4 seep plume from 70 m. Seabed normalized volume averaged over depth window ($<Q>$) of the rising bubble plume for **b.** calibration plume, and **e.** seep plume. Molar vertical flux for **c.** calibration plume, and **f.** seep Data keys on panels.

There are dramatic changes in the size distribution of a pure CH_4 minor seep bubble plume rising from 70-m depth with the smallest bubbles dissolving and the largest bubbles growing (**Fig. 10d**). Overall, air uptake and decreasing hydrostatic pressure largely balance dissolution for the plume overall for the first 50 m of bubble rise and $<Q_z>$ remains roughly stable (**Fig. 10e**) – Q decreases by 0.7%, 0.2%, and 0.0% in the first three 5-meter depth windows, respectively. Note, stable Q does not imply constant total CH_4 bubble content, which continually outflows the rising bubble.

Thus, the volume correction factors between the calibration-plume and the seep plume are 0.948, 0.868, and 0.775 for the 65-70, 60-65, and 55-60 m depth windows, respectively. Thus, the calibration plume *Q* averaged over the 35-40 m depth window is ~5% greater than the seep bubble plume *Q* for the 70-65 m depth window.

3.3. Natural Seepage

The depth-dependent calibration was applied to MBES and SBES sonar data collected in the Laptev Sea for 70-m deep seepage under conditions of strong currents (**Fig. 11**). Three seep areas were surveyed, two weak and one strong, all with numerous plumes. The MBES data illustrates the additional spatial information missing in SBES systems. For example, Seep Area 1 in the SBES data (**Fig. 11b**) appears to show extensive diffuse seepage, which the MBES data (**Fig. 11a**) reveal arises from many low-flow discrete bubble plumes.

The flux for the seep areas (**Fig. 12**) was mapped by averaging the seepage flux in the 65-70 m depth window in 1-m^2 quadrats after application of the calibration curves and correction factors. The deepest depth window was chosen to preserve better the seabed location of emissions for spatial analysis.

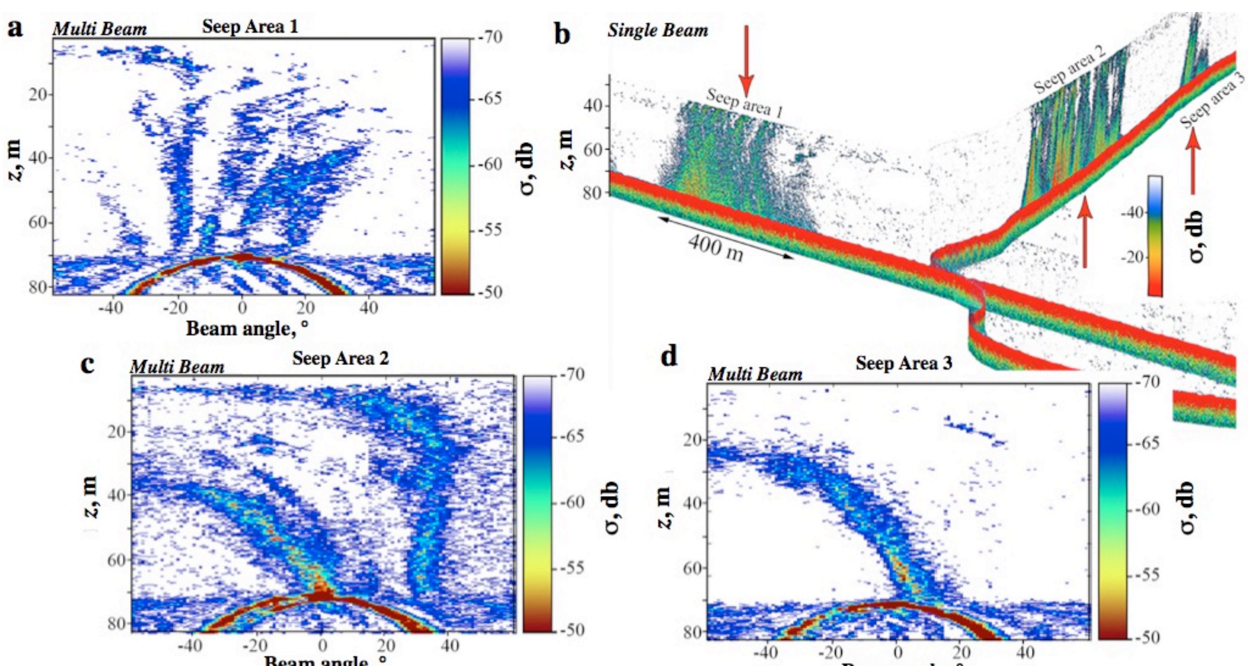

Figure 11. Sonar return, s, with depth, *z*, of seep bubble plumes in the Laptev Sea. **a. c. d.** Multibeam sonar data, single ping, in each of the seep areas, locations labeled on b. **b.** Single beam sonar data. Size scale and data key on panels.

Seep Area 2 was stronger than the other seep areas by an order of magnitude and clearly showed a northeast-southwest trend, which also is apparent in all seep areas. Note, some of the striation patterns, primarily of the weaker returns, are consistent with the very strong currents detraining small bubbles out of the plume in the direction of the sonar beam fan. On a second, east-west leg, Seep Area 1 was surveyed with currents not-aligned with the sonar beam fan and does not exhibit the striation. Further evidence of the effect of currents is shown in the sonar ping data (**Fig. 12b vs. Figs. 12c and 12d**); where Seep Area 1 does not show the extreme tilt across beams as in sonar data for Seep Areas 2 and 3. Thus, the linear seep trends must reflect geological control.

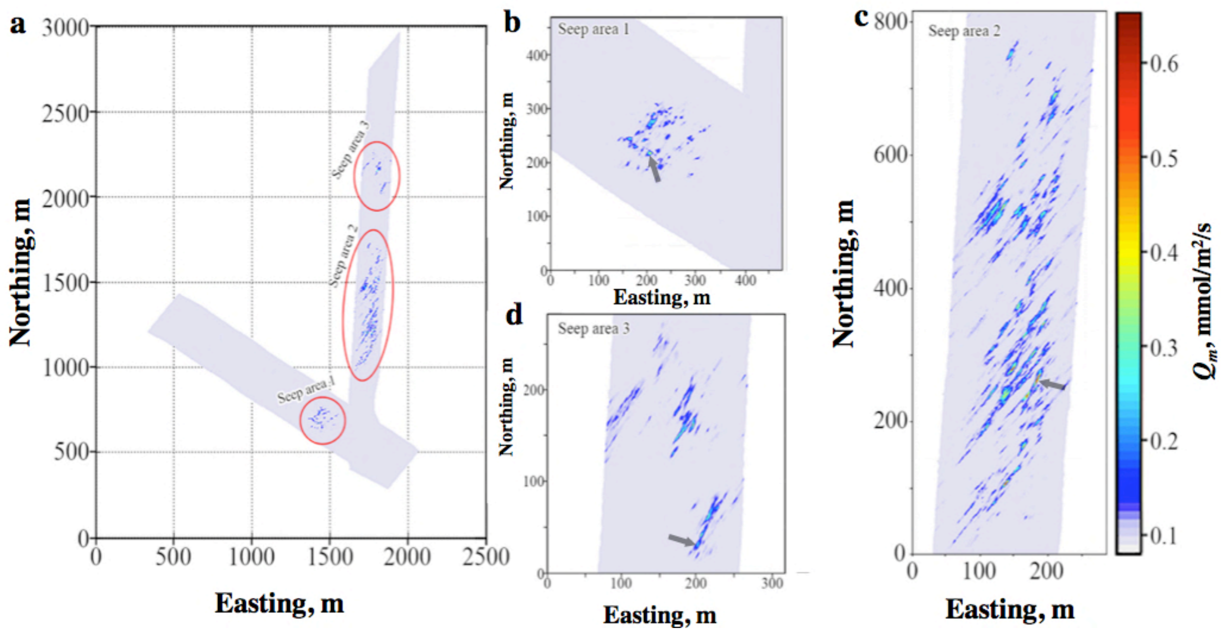

Figure 12. Seep mass flux (Q_m) map for **a** all seep areas, and for **b-d** Seep Areas 1-3. Data key on panel c. Fits in Table 2.

Seepage spatial structure showed numerous seeps clustered around the strongest seep with an apparent modulation at distances of ~100 m (**Supp. Fig. S5**). In seepage areas 1 and 2 the dominant seep plumes were as strong as 0.3 mmol m^{-2} s^{-1} (7.4 cm^3 s^{-1}) while the dominant seep plumes in the stronger Seep Area 2 (**Fig. 12c**) released >0.6 mmol m^{-2} s^{-1} (15 cm^3 s^{-1}).

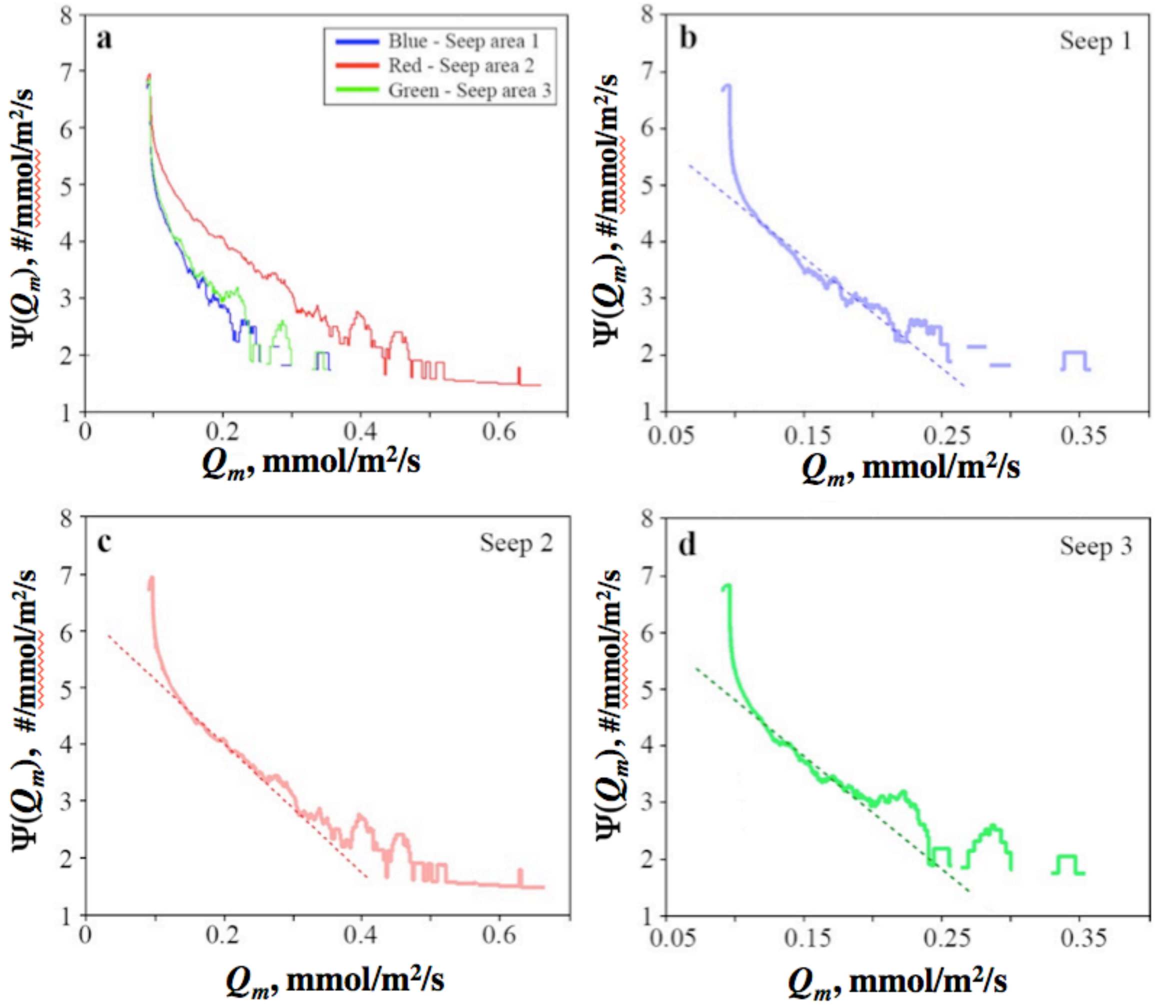

Figure 13. Seep mass flux (Q_m) occurrence probability distribution function ($\Psi(Q_m)$) normalized to flux bin-width (bin widths are logarithmically-spaced) for **a** all seep areas, and for **b-d** Seep Areas 1-3 with power law fits. Data key on panel a. Fits in Table 2.

The mass flux (Q_m) occurrence probability distribution function ($\Psi(Q_m)$) was calculated for each seep area and showed Seep Area 2 contained the largest number of strong seep plumes followed by Seep Area 3 and then Seep Area 1 (**Fig. 13**). For the three areas, $\Psi(Q_m)$ for weak emissions asymptotically approached ~0.1 mmol/m^2/s (2.5 cm^3/s) for all seep areas–the noise level. Thus, the calibration flows (**Fig. 9**) bracketed from the MBES noise level to the largest observed seep plume. Seep Area 2 exhibits both greater fluxes and a shallower power law (**Fig. 13c**). Furthermore, all three seep areas exhibited positive anomalies or peaks in $\Psi(Q_m)$ for stronger flux seepage. These peaks signify a preferred emission mode–i.e., multiple seeps with similar emission fluxes. For weaker seeps with good signal to noise ($Q_m >$ 0.15 mmol/m^2/s), the power law fits are nearly identical, 6.65, 6.27, 6.80 (**Table 2**) for Seep Areas 1, 2, 3, respectively.

Total flux in each seep area was determined by area integration and was 5.56, 42.73, and 4.88 mmol/s for the MBES data (**Table 2**). SBES-derived emissions were biased lower compared to MBES, by 3.7% - 36% for the seep areas, with best agreement for Seep Area 2.

TABLE 2 HERE

4. Discussion

4.1. Bubble-Bubble Acoustic Interaction

We presented results of an *in situ* engineered bubble plume experiment to investigate the evolution of bubble plume sonar return for flows spanning two orders of magnitude. This range was comparable to typical low flow minor plumes and very strong high flow major plumes (Leifer, 2010). Calibration plume sonar return increased strongly and non-linearly with flux, ~15 db for a flow doubling from 0.02 to 0.04 L/s. This increase is faster than the 6 db increase that would be expected by simply summing the sonar cross sections of the doubled number of bubbles. Instead, the increase suggests strong bubble-bubble acoustical interactions. Specifically, with increased flow, overall plume dimensions expand more quickly, leading to less bubble shadowing and shallower sonar occurrence probability distribution function slopes at the same height above the nozzle (**Fig. 9**). In contrast to the overall plume dimensions (which includes smaller more dispersed bubbles) the dense core of large bubbles tends not to disperse and is largely insensitive to height (**Fig. 9**). Thus, for the dense core, increased flux increases bubble shadowing such that the signal of the additional bubbles is blocked by other bubbles and sonar return becomes nearly independent of flow, i.e., saturated (**Figs. 9a and 9b**). Similar saturation is apparent in the data presented in Greinert and Nützel (2004) for an air bubble plume in far shallower water. Thus, the calibration data provides strong evidence of non-negligible bubble-bubble acoustical interaction at both low and high flow rates. Furthermore, the relationship's non-linearity is shown in the trend of $\sigma(z,Q)$ as the bubble plume rises and disperses. Thus, bubble-bubble acoustic interactions remain significant even after the plume has risen 15 m.

As a high-flow bubble plume rises, the weak σ portion of the plume representing small bubbles dispersed, leading to an increase in the integrated σ, as was observed in the Coal Oil Point (COP) and ESAS engineered plume data. In the COP seep field study, calibration flows extended from comparable to far higher flows than those in the ESAS, and documented that sonar return increased with height on fine depth scales (**Fig. 6**). This was interpreted as due to decreasing bubble "shadowing" of more distant bubbles as the plume expands and becomes more diffuse. As the ESAS engineered plumes rose, the sonar occurrence probability distribution function showed a strong influence from small bubble dispersion as the plume expanded and an increase in the integrated σ (**Fig. 9**)

As low-flow calibration plumes rise and disperse, sonar return decreases. Overlapping intermediate depth windows were evaluated and confirmed this was not an artifact of plume oscillatory motions aliasing the return signal across the depth windows. The decrease in integrated sonar return with rise is (by definition) a decrease in scattered sonar energy, i.e., greater energy scatters back to the sonar when the plume is spatially denser. This could arise from a decrease in shadowing, or dissolution; however, the bubble model showed that minor plume dissolution did not change overall plume volume significantly (**Fig. 10**), unlike the significant changes in integrated σ, e.g., **Fig. 8c**.

4.2 Bubble Detrainment and Bubble-Bubble Acoustic Interaction

The artifact striations in the natural seep sonar data from currents are consistent with non-negligible bubble-bubble acoustic interaction (**Fig. 12**). Specifically, seep bubble plumes were imaged for high currents that advected small bubbles out of the plumes into the downcurrent water. When these were in the orientation of the beam fan, they were observed, but not when the beam fan was perpendicular to the currents. For co-orientation of the beam fan and currents, scattered acoustic energy interacts with nearby downcurrent bubbles, which remain in the beam. This arises because the cross-track beam dimension is very broad (120°), while the along-track beam width is very narrow – a few degrees. Thus, when cross-oriented, the sonar beam fan fails to image the detrained bubbles. This provides clear evidence of bubble-bubble acoustic sonar interactions at larger distances than the plume dimensions.

4.3. Bubble Size Distribution

Bubble size distributions have been reported for other ESAS seep sites (Shakhova et al., 2015), but equipment to make such measurements were unavailable for this study. Bubble modeling was used to address the effect of evolving bubble size distribution with flow in application of calibration air or nitrogen (preferred for safety reasons over methane) bubble plumes to seep bubble plumes (**Fig. 10**). In this study, we applied a first approximation using a typical minor bubble plume size distribution. Clearly initializing the model with measured plumes would improve the accuracy of the volume correction factor and hence sonar-derived flux. Still, the primary goal in our study is to demonstrate with a simple approximation that bubble size matters and should not be neglected.

Although the simulations were conducted to correct between a nitrogen calibration plume and pure methane seep bubbles, if the seep bubbles contained other gases at non-trace levels, their outgassing could impact significantly bubble size evolution. In particular, carbon dioxide (CO_2), which is far more soluble than methane, can lead to rapid bubble size change, primarily in the deepest depth windows, e.g., see CO_2 plume simulation in Leifer et al. (2015). Additionally greater sensitivity arises from the depth of the bubble plume (Leifer and Patro, 2002), thus, the depth discrepancy between calibration and seep plumes should be minimized. Future calibration studies also should account for size distribution and upwelling flow with respect to flow rate.

4.4. Field comparison of MBES with SBES

The MBES and SBES systems were calibrated with the same nitrogen gas bubble plumes, thus the two systems should agree in terms of flux observations. Calibration flows spanned very weak flow (Q = 0.19 L/s) to very strong flows (Q = 1.1 L/s). The low-flow calibration bubble plume (**Fig. 9**) was less than the seep field noise floor of the MBES system (**Fig. 13**), while the high flow was more than an order of magnitude greater than field observations.

Field observations showed far better agreement between systems for Seep Area 2 than the other seep areas (Table 2). This most likely relates to the greater relative importance of stronger seeps that are well above the noise level relative to the other seep areas. The calibration flows (**Fig. 9**) showed weaker sonar return for the SBES than for the MBES for the same flow. Geometric uncertainty likely also played a role in a downward flux bias of the SBES.

4.5. Seepage Spatial Characterization

The seepage spatial and strength distribution in the ESAS (**Fig. 12**) share similarities with structures in the COP seep field (**Fig. 1**). Subsurface geologic structures control the seepage spatial-flux distribution by creating the pathways through which seepage migrates to the seabed and ocean - seepage areas must occur where geologic structures allow. In the COP seep field, strong seepage areas are located at intersecting non-compressional faults and fractures (Leifer et al., 2010). Furthermore, these faults and/or fractures themselves are preferred migration pathways that connect subsurface reservoirs to the seabed, with seepage tending to manifest along their trend.

In the ESAS seepage map (**Fig. 12**), two spatial trends were manifest, one northeast-southwest of individual vents and second a north-south elongation in Seep Area 2. Both trends were aligned with the two weaker seepage areas. Furthermore, the northeast-southwest trend is apparent within Seep Area 2. Here, fractures in submerged permafrost could play a similar role to the role of fault intersections in the COP seep field; however, more extensive seep area mapping is needed for validation, and/or penetrating sonar data that can image near surface rock strata. On smaller length scales, there is an evident striation pattern in vent locations suggesting a subsurface linear geological control on meter length scales.

High flow seepage requires high permeability migration pathways, while low flow seepage occurs along low permeability migration pathways if the driving pressure between the deeper reservoir and the seabed is constant across the active seepage area (Leifer and Boles, 2005). Thus, the stronger and more numerous and extensive seepage emissions from Seep Area 2 indicates higher subsurface permeability and subsurface connectivity with more numerous migration pathways than the other seep areas (**Fig. 12**). Seepage connectivity can be envisioned topologically as an inverted branched structure (Leifer and Boles, 2005) where central stronger seepage is surrounded (generally) by weaker seepage (**Supp. Fig. S6**). Given that permeability is inversely related to resistance in the migration pathways, stronger seepage is fed by migration along pathway(s) with lower resistance (higher permeability), while weaker seepage is fed by migration along pathways with stronger resistance (lower permeability). One implication of a range of migration pathways with different resistance is that lower resistance seepage adjusts to changes in seepage easier than higher resistance seepage – thus strong seeps become stronger, while weak seeps are more likely to activate/deactivate with changes in emissions (Bradley et al., 2010). The balance between seepage emissions for different migration pathways with a range of permeability underlies the flux probability distribution function shown in **Fig. 12**.

The mapped seepage emissions demonstrated highly similar geologic spatio-flux control. Specifically, weak seepage flux exhibited a power law exponent (b) of -6 (**Fig. 12**). This power law describes how the seepage is distributed between high and low permeability migration pathways. Note, the actual power law likely is exaggerated slightly from bubble detrainment into the beam fan in Seep Areas 2 and 3, which spreads sonar return spatially; however, Seep Area 1 does not have this beam fan effect, yet exhibited a similar b to the other areas. This argues that the shallow seabed structure (fracture, porosity, etc.) related to low permeability migration pathways is common across the areas, with the main controlling factor being the number of bubbles escaping per second per unit area of seabed.

This power law does not extend to the largest seep fluxes, which manifest as perturbations (peaks) above the b=-6 power law in the flux probability distribution function. Higher flow plumes, and thus high permeability pathways, could represent a failure of the normal seabed structure (that governs the weak seepage) from stresses and/or talik melting, leading to focused high flow migration pathways that help define where the seep areas lie.

In the Arctic, subsea permafrost degradation from heating both below (geologic – most strong in faulted zones) and above (riverine inputs and overall Arctic Ocean warming) creates migration pathways that manifest as seep spatio-flux distributions. The presence of active seepage in this region likely relates to these heat flows, with the hotspots likely related to taliks and/or subsea thaw lakes, whose locations are controlled by linear geologic structures. In the ESAS, grabens are often linear structures, which often are correlated with paleo-river valleys, and could cause co-aligned fractures controlling seepage along linear trends. The similarity in the emission probability distribution power law (b=-6) indicates that subsurface permeability exhibits a fractal distribution that is similar between the three areas – arguing for similar formation mechanism, i.e., taliks. In this case, at the intersection of the two linear trends, where fluid migration thus heat flow likely are higher, leading to more rapid talik development providing high permeability migration pathways.

4.6. Broader Implications

There are enormous carbon stores sequestered in marine-permafrost in the Arctic, which are of particular concern for release as the warming Arctic Oceans transfer heat faster than from the atmosphere to terrestrial permafrost. Migration from this submerged permafrost reservoir to the ocean has created a vast marine seep field that lies entirely in shallow waters with emissions contributing directly to atmospheric budget (Shakhova et al., 2014). Widespread ESAS seabed bubble emissions have been documented (Shakhova et al., 2014; Shakhova et al., 2015) demonstrating failure of the permafrost's integrity and making methane and additional organic carbon available for microbial methane generation.

These observations support the hypothesis that the current state of sub-sea permafrost is a controlling factor to the spatial variability in methane seabed fluxes, and is undergoing destabilization from warming (Shakhova et al., 2010a; Shakhova et al., 2010b). The current state of subsea permafrost beneath the ESAS is a potential key to understanding whether and how, methane preserved in seabed reservoirs, escapes to atmosphere. Currently our state of knowledge engenders enormous uncertainty in future emissions in large part due to the paucity of data. Among the new tools and techniques needed to evaluate these fluxes quantitatively over wide areas, *in situ* calibrated sonar shows significant promise.

4.7. Future Directions

In this study, bubble plume spanning almost two orders of magnitude, from 0.019 to 1.1 L/s were engineered; however, a key intermediate range (0.045-0.8 L/s) was missed. This is the regime where bubble plumes shifts from a non-linear relationship between sonar return and flow to saturation where sonar return is largely independent of flow. Furthermore, experiments should follow the calibration plumes for more than 15 m; however, currents made this infeasible. Although, calibration plumes were isolated bubble plumes, seep bubble plumes often escape from nearby vents into plumes that eventually merge. Given the importance of bubble-bubble acoustic interactions, calibration studies should compare the same total flux from single source with that from several closely-located bubble sources to investigate whether there is convergence between single bubble plumes and multiple bubble plumes with rise height as the plume merge. Finally, studies in calmer waters could elucidate better the importance of small bubbles versus large bubbles to overall sonar return.

This study featured the novel use of a numerical bubble plume model to correct for different size evolution between calibration gas bubble plumes and seep bubble plumes. Uncertainty arises from the bubble size distribution, which needs to be measured for the calibration and seep bubble plumes at multiple flow rates. Our approach was a simplified first effort with room for improvement, including measurement of bubble size distributions in the field.

5. Conclusions

In this study, using the calibrated multi-beam and single-beam sonars, we present a methodology of using an in situ plume calibration approach to derive quantitative sonar methane emissions maps from the Laptev Sea outer shelf where subsea permafrost has presumably degraded the most according modeling results. We created in situ engineered bubble plumes from 40-m depth spanning almost two orders of magnitude – from 0.019 to 1.1 L/s. Non-linear curves relating sonar return to flux for a range of depths demonstrated significant bubble-bubble acoustic interactions, which precludes an inversion approach based on scaling bubble sonar cross section with the size distribution. Analysis of the depth evolution of the bubble plume sonar occurrence probability distribution function for different fluxes found weak sonar return was well described by a power law that likely correlated with small bubble dispersion, while strong sonar returns largely were independent of depth, consistent with a focused central core of large bubbles. As a result, plume sonar occurrence probability distribution function was bimodal for all but the weakest seepage.

The *in situ* calibration curve was applied to a natural seepage area from 70-m depth after accounting for the different volume evolution of the nitrogen calibration plume and the methane seep bubble plume through use of a numerical bubble plume model initialized with a typical (assumed) minor bubble plume size distribution. The bubble model suggested an ~5% correction between the two plumes for the first 5-m depth window. Three nearby seepage areas with total emissions of 5.56, 42.73, and 4.88 mmol/s from multibeam sonar data were mapped, with good to reasonable agreement (4-37%) between single and multibeam sonar, although single beam emissions were biased lower. Seepage occurrence probability distribution function was bimodal, with weak seepage occurrence probability distribution function in each seep area well described by a power law. This was interpreted as suggesting primarily small minor bubble plumes, while a few stronger seepage plumes were mapped that could be major plumes. Seepage mapped spatial patterns suggested subsurface geologic control along linear trends.

6. Acknowledgements

We thank the crew and personnel of the expedition onboard research vessel *Victor Buinitsky*. We would like to acknowledge financial support from the Government of the Russian Federation (Grant #14, Z50.31.0012/03.19.2014), the Far Eastern Branch of the Russian Academy of Sciences (FEBRAS). At different stages work was supported by the US National Science Foundation (OPP ARC -1023281), the US National Oceanic and Atmospheric Administration (Siberian Shelf Study), Russian Foundation for Basic Research (grants #13-05-12028 and 13-05-12041), and Headquarters of the Russian Academy of Sciences (Arctic Program led by A.I. Khanchuk). N. S. and D. C. acknowledge the Russian Scientific Foundation (grant #15-17-20032).

Tables

Table 1. Integrated depth-windowed methane flux estimates.

Designation	$Q_{m\text{-SBES}}$* (mmol/m^2/s)	S$Q_{m\text{-SBES}}$ (mmol/s)	$Q_{m\text{-MBES}}$** (mmol//m^2/s)	S$Q_{m\text{-MBES}}$ (mmol/s)	Area (km^2)	E (%)	S$Q_{m\text{-MBES}}$ (L/s)
Seep 1	0.22	3.78	0.33	5.56	0.017	32	0.14
Seep 2	0.59	41.16	0.61	42.73	0.070	3.7	1.07
Seep 3	0.26	3.96	0.33	4.88	0.015	19	0.12

Q is volume flux, Q_m is mass flux, U is uncertainty, where E=($Q_{m\text{-}MBES}$-$Q_{m\text{-}SBES}$)/$Q_{m\text{-}MBES}$

*SBES – Single Beam Echosounder, 65-70 m, depth window.

**MBES – Multibeam Echosounder, 65-70 m, depth window.

Table 2. Fit parameters for seep area flux probability distribution function.

Name	$Q_{m\text{-}1}$* (mmol/m^2/s)	$Q_{m\text{-}2}$ (mmol/m^2/s)	a (-)	b (mmol/m^2/s)	R^2
Seep Area 1	0.1	0.2	-19.53	6.648	0.836
Seep Area 2	0.1	0.3	-11.34	6.27	0.9228
Seep Area 3	0.1	0.2	-19.85	6.798	0.8258

Fit from $Q_{m\text{-}1}$ *to* $Q_{m\text{-}2}$, where Q_m is the mass flux rate

References

Archer, D. and Buffett, B.: Time-dependent response of the global ocean clathrate reservoir to climatic and anthropogenic forcing, Geochem. Geophys. Geosyst., 6, Q03002,, 2005.

Asaeda, T. and Imberger, J.: Structure of bubble plumes in linearly stratified environments, Journal of Fluid Mechanics, 249, 35-57, 1993.

Bauch, H. A., Mueller-Lupp, T., Taldenkova, E., Spielhagen, R. F., Kassens, H., Grootes, P. M., Thiede, J., Heinemeier, J., and Petryashov, V. V.: Chronology of the Holocene transgression at the North Siberian margin, Global and Planetary Change, 31, 125-139, 2001.

Biastoch, A., Treude, T., Rupke, L. H., Riebesell, U., Roth, C., Burwicz, E. B., Park, W., Latif, M., Boning, C. w., Madec, G., and Wallman, K.: Rising Arctic Ocean temperatures cause gas hydrate destabilization and ocean acidification, Geophysical Research Letters, 38, L08602, 2011.

Bradley, E. S., Leifer, I., and Roberts, D. A.: Long-term monitoring of a marine geologic hydrocarbon source by a coastal air pollution station in Southern California, Atmospheric Environments, 44, 4973-4981, 2010.

Clark, J. F., Schwager, K., and Washburn, L.: Variability of gas composition and flux intensity in natural marine hydrocarbon seeps. New Energy Development and Technology (EDT) Working Paper 008, UCEI, 15 pp., 2005.

Clark, J. F., Washburn, L., Hornafius, J. S., and Luyendyk, B. P.: Dissolved hydrocarbon flux from natural marine seeps to the southern California Bight, Journal of Geophysical Research, 105, C5, 2000.

Clift, R., Grace, J. R., and Weber, M. E.: Bubbles, Drops, and Particles, Academic Press, New York, 1978.

Dickens, G. R.: Rethinking the global carbon cycle with a large, dynamic and microbially mediated gas hydrate capacitor, Earth and Planetary Science Letters, 213, 169-183, 2003.

Drachev, S. S., Kaul, N., and Beliaev, V. N.: Eurasia spreading basin to Laptev Shelf transition: structural pattern and heat flow, Geophysical Journal International, 152, 688-698, 2003.

Friedlingstein, P., Cox, P., Betts, R., Bopp, L., von Bloh, W., Brovkin, V., Cadule, P., Doney, S., Eby, M., Fung, I., Bala, G., John, J., Jones, C., Joos, F., Kato, T., Kawamiya, M., Knorr, W., Lindsay, K., Matthews, H. D., Raddatz, T., Rayner, P., Reick, C., Roeckner, E., Schnitzler, K. G., Schnur, R., Strassmann, K., Weaver, A. J., Yoshikawa, C., and Zeng, N.: Climate–carbon cycle feedback analysis: Results from the C4MIP model intercomparison, Journal of Climate, 19, 3337-3353, 2006.

Gautier, D. L., Bird, K. J., Charpentier, R. R., Grantz, A., Houseknecht, D. W., Klett, T. R., Moore, T. E., Pitman, J. K., Schenk, C. J., and Schuenemeyer, J. H.: Assessment of undiscovered oil and gas in the Arctic, Science, 324, 1175-1179, 2009.

Gramberg, I. S., Kulakov, Y. N., Pogrebitsky, Y. E., and Sorokov, D. S.: Arctic oil and gas super basin, X World Petroleum Congress, London, 93-99, 1983.

Graversen, R. G., Mauritsen, T., Tjernstrom, M., Kallen, E., and Svensson, G.: Vertical structure of recent Arctic warming, Nature, 451, 53-56, 2008.

Greinert, J., McGinnis, D. F., Naudts, L., Linke, P., and De Batist, M.: Atmospheric methane flux from bubbling seeps: Spatially extrapolated quantification from a Black Sea shelf area, Journal of Geophysical Research, 115, 2010.

Greinert, J. and Nützel, B.: Hydroacoustic experiments to establish a method for the determination of methane bubble fluxes at cold seeps, Geo-Marine Letters, 24, 75-85, 2004.

Hölemann, J. A., Kirillov, S., Klagge, T., Novikhin, A., Kassens, H., and Timokhov, L.: Near-bottom water warming in the Laptev Sea in response to atmospheric and sea-ice conditions in 2007, 2011, doi: 10.3402/polar.v30i0.6425, 2011. 2011.

Hornafius, S. J., Quigley, D. C., and Luyendyk, B. P.: The world's most spectacular marine hydrocarbons seeps (Coal Oil Point, Santa Barbara Channel, California): Quantification of emissions, Journal Geophysical Research - Oceans, 104, 20703-20711, 1999.

Judd, A. and Hovland, M.: Seabed fluid flow: The impact on geology, biology and the marine environment, Cambridge University Press, 2007.

Leifer, I.: Characteristics and scaling of bubble plumes from marine hydrocarbon seepage in the Coal Oil Point seep field, Journal Geophysical Research, 115, C11014, 2010.

Leifer, I. and Boles, J.: Measurement of marine hydrocarbon seep flow through fractured rock and unconsolidated sediment, Marine and Petroleum Geology, 22, 551-568, 2005.

Leifer, I. and Culling, D.: Formation of seep bubble plumes in the Coal Oil Point seep field, Geo-Marine Letters, 30, 339-353, 2010.

Leifer, I., Jeuthe, H., Gjøsund, S. H., and Johansen, V.: Engineered and natural marine seep, bubble-driven buoyancy flows, Journal of Physical Oceanography, 39, 3071-3090, 2009.

Leifer, I., Kamerling, M., Luyendyk, B. P., and Wilson, D.: Geologic control of natural marine hydrocarbon seep emissions, Coal Oil Point seep field, California, Geo-Marine Letters, 30, 331-338, 2010.

Leifer, I., Luyendyk, B. P., Boles, J., and Clark, J. F.: Natural marine seepage blowout: Contribution to atmospheric methane, Global Biogeochemical Cycles, 20, GB3008, 2006.

Leifer, I. and Patro, R.: The bubble mechanism for methane transport from the shallow sea bed to the surface: A review and sensitivity study, Continental Shelf Research, 22, 2409-2428, 2002.

Leifer, I., Solomon, E., Schneider v. Deimling, J., Coffin, R., Rehder, G., and Linke, P.: The fate of bubbles in a large, intense bubble plume for stratified and unstratified water: Numerical simulations of 22/4b expedition field data, Journal of Marine and Petroleum Geology, 68B, 806-823, 2015.

Leifer, I. and Tang, D. J.: The acoustic signature of marine seep bubbles, Journal of the Acoustical Society of America, Express Letters, 121, EL35-EL40, 2006.

Lemke, P., Ren, J., Alley, R. B., Allison, I., Carrasco, J., Flato, G., Fujii, Y., Kaser, G., Mote, P., Thomas, R. H., and Zhang, T.: Observations: Changes in Snow, Ice and Frozen Ground. In: Climate change 2007 : The physical science basis, Contribution of Working Group 1 to the Fourth Assessment Report of the Intergovernmental Panel on Climate Change, Solomon, S., Qin, D., Manning, M., Chen, Z., Marquis, M., Averyt, K. B., Tignor, M., and Miller, H. L. (Eds.), Cambridge University Press, Cambridge, UK, 2007.

MacDonald, I.: Remote sensing and sea-truth measurements of methane flux to the atmosphere (HYFLUX project), US Department of Energy, National Energy Technology Laboratory,, 164 pp., 2011.

Makogon, Y. F., Holditch, S. A., and Makogon, T. Y.: Natural gas hydrates - A potential energy source for the 21st Century, Journal of Petroleum Science and Engineering, 56, 14-31, 2007.

Maksimov, A. O., Burov, B. A., Salomatin, A. S., and Chernykh, D. V.: Sounds of undersea gas leaks. In: Underwater Acoustics and Ocean Dynamics: Proceedings of the 4th Pacific Rim Underwater Acoustics Conference, Zhou, L., Xu, W., Cheng, Q., and Zhao, H. (Eds.), Springer Singapore, Singapore, 2016.

Minnaert, M.: On musical air bubbles and the sound of running water, Philosophical Magazine, 16, 235-248, 1933.

Nicolsky, D. and Shakhova, N.: Modeling sub-sea permafrost in the East-Siberian Arctic Shelf: the Dmitry Laptev Strait, Environmental Research Letters, 5, 2010.

Nicolsky, D. J., Romanovsky, V. E., Romanovskii, N., Kholodov, A. L., Shakhova, N. E., and Semiletov, I.: Modeling sub-sea permafrost in the East Siberian Arctic Shelf: The Laptev Sea region, Journal of Geophysical Research, 117, F03028, 2012.

Osterkamp, T. E.: Subsea Permafrost. In: Climate and Oceans, John H. Steele, Steve A. Thorpe, and Turekian, K. K. (Eds.), Academic Press, London UK, 2010.

Pugach, S. P., Pipko, I. I., Semiletov, I. P., and Sergienko, V. I.: Optical characteristics of the colored dissolved organic matter on the East Siberian shelf, Doklady Earth Sciences, 465, 1293-1296, 2015.

Rehder, G., Keir, R. S., Suess, E., and Rhein, M.: Methane in the Northern Atlantic controlled by microbial oxidation and atmospheric history, Geophysical Research Letters, 26, 587-590, 1999.

Rehder, G., Leifer, I., Brewer, P. G., Friederich, G., and Peltzer, E. T.: Controls on methane bubble dissolution inside and outside the hydrate stability field from open ocean field experiments and numerical modeling, Marine Chemistry, 114, 19-30, 2009.

Romanovskii, N. N., Hubberten, H.-W., Gavrilov, A. V., Eliseeva, A. A., and Tipenko, G. S.:

Offshore permafrost and gas hydrate stability zone on the shelf of East Siberian Seas, Geo-Marine Letters, 25, 167-182, 2005.

Römer, M., Sahling, H., Pape, T., Bohrmann, G., and Spieß, V.: Quantification of gas bubble emissions from submarine hydrocarbon seeps at the Makran continental margin (offshore Pakistan), Journal of Geophysical Research: Oceans, 117, C10015, 2012.

Sahling, H., Bohrmann, G., Artemov, Y., G.,, Bahr, A., Brüning, M., Klapp, S., A.,, Klaucke, I., Kozlova, E., Nikolovska, A., Pape, T., Reitz, A., and Wallmann, K.: Vodyanitskii mud volcano, Sorokin trough, Black Sea: Geological characterization and quantification of gas bubble streams, Marine and Petroleum Geology, 26, 1799-1811, 2009.

Schneider von Deimling, J., Brockhoff, J., and Greinert, J.: Flare imaging with multibeam systems: Data processing for bubble detection at seeps, Geochemistry, Geophysics, Geosystems, 8, 1-7, 2007.

Schneider von Deimling, J., Greinert, J., Chapman N.R., Rabbel, W., and Linke, P.: Acoustic imaging of natural gas seepage in the North Sea: Sensing bubbles controlled by variable currents, Limnology and Oceanography Methods, 8, 155-171, 2010.

Schneider von Deimling, J., Rehder, G., Greinert, J., McGinnis, D. F., Boetius, A., and Linke, P.: Quantification of seep-related methane gas emissions at Tommeliten, North Sea, Continental Shelf Research, 31, 867-878, 2011.

Semiletov, I., Pipko, I., Gustafsson, O., Anderson, L. G., Sergienko, V., Pugach, S., Dudarev, O., Charkin, A., Gukov, A., Broder, L., Andersson, A., Spivak, E., and Shakhova, N.: Acidification of East Siberian Arctic Shelf waters through addition of freshwater and terrestrial carbon, Nature Geosci, 9, 361-365, 2016.

Semiletov, I. P., Shakhova, N. E., Pipko, I. I., Pugach, S. P., Charkin, A. N., Dudarev, O. V., Kosmach, D. A., and Nishino, S.: Space–time dynamics of carbon and environmental parameters related to carbon dioxide emissions in the Buor-Khaya Bay and adjacent part of the Laptev Sea, Biogeosciences, 10, 5977-5996, 2013.

Semiletov, I. P., Shakhova, N. E., Sergienko, V. I., Pipko, I. I., and Dudarev, O. V.: On carbon transport and fate in the East Siberian Arctic land-shelf-atmosphere system, Environmental Research Letters, 7, 2012.

Serreze, K. C., Stroeve, J., Mauritzen, C., Cazenave, A., Rignot, E., Bates, N. R., Canadell, J. G., Raupach, M. R., Shakhova, N., and Semiletov, I.: Arctic climate feedbacks: Global implications, World Wildlife Foundation, 98 pp., 2009.

Shakhova, N., Nicolsky, D. J., and Semiletov, I. P.: On the current state of sub-sea permafrost in the East-Siberian Shelf testing of modeling results by observational data, Transactions of Russian Academy of Sciences, 429, 2009.

Shakhova, N. and Semiletov, I.: Methane release and coastal environment in the East Siberian Arctic Shelf, Journal of Marine Systems, 66, 227-243, 2007.

Shakhova, N., Semiletov, I., Leifer, I., Rekant, P., Salyuk, A., and Kosmach, D.: Geochemical and geophysical evidence of methane release over the East Siberian Arctic Shelf, Journal of Geophysical Research., 115, C08007, 2010a.

Shakhova, N., Semiletov, I., Salyuk, A., Iossoupov, V., Kosmach, D., and Gustafsson, O.: Extensive methane venting to the atmosphere from sediments of the East Siberian Arctic Shelf, Science, 327, 1246-1249, 2010b.

Shakhova, N., Semiletov Igor P., Leifer, I., Sergienko, V., Salyuk, A., Kosmach, D., Chernikh, D., Stubbs, C., Nicolsky, D., Tumskoy, V., Alexeev, V., and Gustafsson, O.: Ebullition and storm-induced methane release from the East Siberian Arctic Shelf, Nature Geoscience, 7, 64-70, 2014.

Shakhova, N., Semiletov Igor P., Valentin Sergienko, Leopold Lobkovsky, Yusupov, V., Salyuk, A., Salomatin, A., Chernykh, D., Kosmach, D., Panteleev, G., Joye, S., Charkin, A., Dudarev, O., Meluzov, A., and Gustafsson, O.: The East Siberian Arctic Shelf: Towards further assessment of permafrost-related methane fluxes and role of sea ice, Philosophical Transactions of the Royal Society A: Mathematical, Physical and Engineering Sciences, 373, 1-13, 2015.

Shakhova, N. E. and Semiletov, I. P.: Methane Hydrate Feedbacks, WWF International Arctic Programme978-2-88085-305-1, 81-92 pp., 2009.

Solomon, E., Kastner, M., MacDonald, I. R., and Leifer, I.: Considerable methane fluxes to the atmosphere from hydrocarbon seeps in the Gulf of Mexico, Nature Geoscience, 2, 561-565, 2009.

Soloviev, V. A., Ginzburg, G. D., Telepnev, E. V., and Mihalyuk, Y. N.: Cryothermia and natural gas hydrates within the Arctic Ocean, Sevmorgeologiya, Leningrad, 1987.

Stubbs, C.: Spatial distribution of near-shore gas seepage from sub-sea permafrost in the Laptev Sea Shelf, Arctic Ocean, MS, Geological Sciences, University of California, Santa Barbara, Santa Barbara, 118 pp., 2010.

Tarnocai, C., Canadell, J. G., Schuur, E. A. G., Kuhry, P., Mazhitova, G., and Zimov, S.: Soil organic carbon pools in the northern circumpolar permafrost region, Global Biogeochemical Cycles, 23, GB2023, 2009.

Tsuchiya, K., Ohsaki, K., and Taguchi, K.: Large and small bubble interaction patterns in a bubble column, International Journal of Multiphase Flow, 22, 121-132, 1996.

Veloso, M., Greinert, J., Mienert, J., and De Batist, M.: A new methodology for quantifying bubble flow rates in deep water using splitbeam echosounders: Examples from the Arctic offshore NW-Svalbard, Limnology and Oceanography: Methods, doi: 10.1002/lom3.10024, 2015. n/a-n/a, 2015.

Warzinski, R. P., Lynn, R., Hasljasmaa, I., Leifer, I., Shaffer, F., Anderson, B. J., and Levine, J. S.: Dynamic morphology of gas hydrate on a methane bubble in water: Observations and new insights for hydrate film models, Geophysical Research Letters, 41, 6841-6847, 2014.

Weber, S. A., Engel-Cox, J. A., Hoff, R. M., Prados, A. I., and Zhang, H.: An improved method for estimating surface fine particle concentrations using seasonally adjusted satellite aerosol optical depth, Journal of the Air & Waste Management Association, 60, 574-585, 2010.

Wilson, D., Leifer, I., and Maillard, E.: Megaplume bubble process visualization by 3D multibeam sonar mapping, Journal of Marine and Petroleum Geology, 68, 753-765, 2015.